Dewatering saturated, networked suspensions with a screw press

Tom S. Eaves · Daniel T. Paterson · Duncan R. Hewitt · Neil J. Balmforth · D. Mark Martinez

Abstract A model is presented for the dewatering of a saturated two-phase medium in a screw press. The model accounts for the detailed two-phase rheological behaviour of the pressed material and splits the press into two zones, an initial well-mixed constant-pressure region followed by an axial transport region in which the total pressure steadily increases. In this latter region, a slowly-varying helical coordinate transformation is introduced to help reduce the dynamics to an annular bi-axial compression of the two-phase medium. Unlike previous modeling, the transition point between the two zones is determined self-consistently, rather than set *a priori*, and the pressure along the length of the press is deduced from the rheology of the two-phase flow rather than averaging the two-phase dynamics over a cross-section of the press. The model is compared to experimental observations of the dewatering of a paper-making fibre suspension and of a clay slurry, and is shown to reproduce operational data.

1 Introduction

Mechanical presses are commonly used to remove water from suspensions in a variety of industrial processes ranging from paper manufacturing to food processing and waste-water treatment [1]. In these devices, material is forced through a geometrical constriction with at least one perforated wall, across which liquid is expelled whilst retaining the majority of the solid constituents. The solid thereby consolidates to a larger solid volume fraction to form a relatively dry 'cake'. One

T. S. Eaves · N. J. Balmforth
Department of Mathematics
University of British Columbia
Vancouver, BC, V6T 1Z2, Canada
E-mail: tse23@math.ubc.ca

D. T. Paterson · D. M. Martinez
Department of Chemical and Biological Engineering
University of British Columbia
Vancouver, BC, V6T 1Z4, Canada

D. R. Hewitt
Department of Applied Mathematics and Theoretical Physics
University of Cambridge
Cambridge, CB3 0WA, UK

common, continuously processing device is the screw press, an example of which is illustrated in figure 1. Such presses consist of a cylindrical, perforated basket within which a helical flight attached to a rotating inner shaft transports material along the press. The geometrical constriction is provided by some combination of an expansion of the radius of the inner shaft and a gradual decrease in the pitch of the helical flight. A counter pressure is exerted on the compacting cake by forcing the material to pass through a narrow exit, created either by the geometry of the press or by inserting a cone at the rear end. Oilseed presses are similar, except that the supplied material is dry, but the initial pressing produces oil which subsequently saturates the solid seed network [2,3].

The screw press in figure 1 is sometimes referred to as an "expeller", in view of its action to remove the constituent fluid from the two-phase material; screw "extruders" have a similar geometry, but have no perforated basket and are used for the processing of single-phase materials [3]. The closed geometry of the extruder can be idealized by unwinding the internal helical chamber and treating that conduit as a converging rectangular channel. This permits one to model the competition between the drag exerted by the stationary basket and rotating shaft, and the increasing pressure associated with the converging channel, given the rheology of the material [4–7].

Although the understanding and control of the pressure distribution during the operation of the screw press expeller is a key aspect of maintaining long-term performance and reducing wear [3], the detailed dynamics during dewatering appears to have never previously been fully identified. A number of previous models of these devices follow models for extruders, but incorporate radial dewatering across the basket *via* some form of Darcy's law [8–10]; the material is again viewed as single phase, and the back pressure along the conduit balances surface drag, with the leakage of water changing the local rheology. Notably, pressure gradients are only taken into account along the conduit, even though the radial pressure gradients that are responsible for driving the water across the basket must be much higher. The two-phase model of Shirato *et al.* [11] does treat such radial gradients, but their model is not closed in that it requires one to specify the pressure distribution along the press at the outset. The goal of the present work is to provide the first detailed two-phase model of the screw press expeller and identify the governing flow dynamics.

During operation, the feed pressure, shaft rotation rate and outlet pressure are typically set (the latter potentially indirectly by setting the position of the cone and therefore the size of the opening at the exit), and the flux of solid material through the press is the output variable [11]. In the design of dewatering screw presses, substantial effort is put into preventing the material from rotating *en masse* with the shaft during the consolidation, requiring instead the material to slip over the shaft and helical flight [2]. Axial flow is usually achieved by tuning of the rate of geometrical compaction or the back pressure from the cone at the rear end, assisted by roughening the basket surface or attaching axially aligned barriers to it. Nevertheless, the residence time of material in the press indicates that there must be substantial rotation in addition to axial motion [11], and studies with radioactive tracers suggest this occurs primarily near the inlet [2]. Further measurements of the pressure distribution within the press indicate that the pressure remains relatively uniform and equal to that of the feed flow over an initial section of the press, before increasing sharply over a later section to the pressure set by the outlet cone [11,9].

Our rationalization of these observations and design principles is that, as material is fed into the screw press, the narrow exit or obstructing cone increases the pressure on the fluid and solid mixture near the end of the press. The elevated fluid pressure sets up a significant radial gradient that drives the suspension against the basket and the fluid across it, compacting the solid and building up the effective network stress. Because the basket is relatively rough but the shaft and flight are smooth, the associated drag forces prevent the suspension from rotating around the
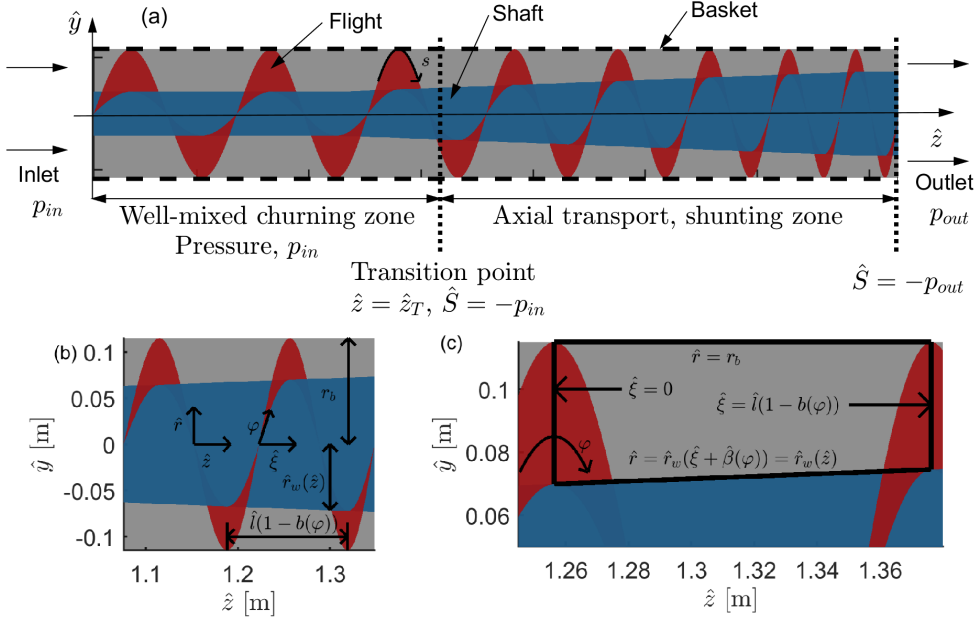
Fig. 1 Sketch of the geometry of a Thule (Voith) SP23 screw press as given in [12] and Appendix B.1, and the two regions of the corresponding idealized model. In detail, (a) shows a plan view. The arc length s follows the meeting point between the flight (red) and the basket (grey). Gradual compression occurs as the flight converges and the shaft (blue) expands along the press. Different regions of the press model developed in §2 are labeled, where the mean network stress $\hat{S}$ is discussed in §2.2. A magnification is shown in (b) along with the global polar coordinates $(\hat{r}, \theta, \hat{z})$; the basket radius is r_b, and the inner shaft radius is $\hat{r}_w(\hat{z})$. Also shown is the local coordinate system $(\hat{r}, \varphi, \hat{\xi})$ at one value of φ; the $\hat{r}$-axis is orthogonal to the local $\hat{\xi}$- and φ-axes, but these latter two axes are not orthogonal. The distance between consecutive turns of the flight with φ separated by 2π is $\hat{l}(1 - b(\varphi))$, where $\hat{l}$ is the basic pitch of the helix in the absence of any convergence of the flight. A further magnification in (c) shows the range of the local coordinates at a given value of φ. Turns of the flight are separated by a distance $\hat{l}(1 - b(\varphi))$ in the $\hat{\xi}$ direction, and $\hat{\xi} = \hat{z} - \hat{\beta}(\varphi)$.

shaft, whilst the normal forces from the flight push the consolidating material down the axis of the press in a "shunting" motion. The consolidation and shunting extend from the outlet back towards the inlet of the press until the net pressure falls to the inlet value, leaving a section near the inlet without significant pressure gradients. Here, the suspension is not sufficiently compressed against the basket to drag the material axially (and may even be unsaturated), implying that the turning of the flight must generate complicated rotational or "churning" motions, that effectively mix the suspension.

Thus, as illustrated in figure 1(a), the dynamics of the press breaks up into two compartments: the shunting zone, where the drag over the basket drives axial motion and consolidation occurs due to the geometrical constriction of the press, and the churning zone, where the inlet pressure is roughly maintained. Although the flow dynamics of the churning zone must be complicated, none of the details need to be incorporated in the model; all that is needed is the assumption that this zone is well mixed with a nearly uniform net pressure. Nevertheless, because water may still be lost through the basket over the churning section, this does imply that the solid fraction over this zone is not equal to that at the inlet and is as yet unknown. However, if the pressure drop across the basket is negligible, the fluid pressure at the onset of shunting must be small (atmospheric). Thus, the inlet pressure of the churning zone must be balanced mainly by the mean network

stress at the beginning of the shunting zone, which dictates the solid volume fraction at the transition point and therefore the water loss over the churning zone. In other words, shunting begins at the position where the material has lost sufficient liquid over the churning section for the effective solid network stress to balance the inlet pressure.

Importantly, in the screw press dynamics summarized above, axial transport is established primarily through normal forces from the flight, guided by the drag on the basket; the simple assumption that the shunting motion is purely axial allows us to omit any details of the underlying mechanical force balance. Crucially, pressure gradients down the helical conduit play no role, divorcing the dynamics from that occurring in the converging channel of a screw extruder; only radial pressure gradients are important, and drive dewatering. Both the onset of shunting and solid flux down the press are determined self-consistently by the balance of the network stress with the inlet pressure at the transition point and matching the back-pressure maintained at the outlet. None of these features are captured simultaneously by extruder-based models [8–11].

To model the screw press, we therefore adopt a two-phase formulation for the material [13], and break the press up into the two compartments. The formulation incorporates Darcy's law for the flow of the fluid; for the solid, we take the effective solid network stress to be given by a plastic compressive yield pressure (as in conventional compaction models [13]) and a rate-dependent viscous term that has proven critical in filtration studies of pulp suspensions [14,15]. Because the churning section has uniform pressure, no detailed model is needed to describe this complicated region; all that is required is the imposition of the conditions holding at the transition point. The dewatering dynamics over the shunting section is described using a slowly-varying helical coordinate transformation [16,6,7], which allows us to exploit the narrowness of the conduit (and the implied dominance of radial gradients) to simplify the governing two-phase equations using an asymptotic expansion (as in conventional lubrication theory [17]). This reduces the problem to that of the bi-axial compression of a two-phase medium within a rectangular slice through the helical conduit due to the slow expansion of the shaft radius and the convergence of the flight. The slower variations along the conduit play no role, save that the corresponding spatial coordinate becomes equivalent to the time variable of a corresponding pressure filtration problem.

Having formulated the theory and made the reduction to our screw press model (in §2), we then examine the dewatering dynamics for some typical operating conditions in addition to detailing the behaviour in the slow and rapid consolidation limits (§3). We also make comparisons to experimental data for materials with or without a rate-dependent solid stress. The results for the case with rate-dependent solid stress are compared with measurements using an industrial-scale paper-making fibre suspension press performed by [12]. In the case without an assumed rate-dependent solid stress, we compare the theoretical predictions with the results of Shirato *et al.* [11], who explored the dewatering of a clay slurry in a laboratory-scale press. In this instance, there are no independent tests that examine the rate-dependence of the solid stress, and we simply assume that none are important, as is standard in work on the consolidation of this type of material. We also explore a simplified bi-axial compression model (in Appendix C) to investigate some general design principles of dewatering screw presses.

2 Two-phase flow in a screw press

2.1 Model description

For this work we consider the input parameters for press operation as the inlet pressure p_{in}, the counter pressure p_{out} at the press exit, and the rotation rate Ω of the shaft-flight assembly. The output variables are the solid flux through the press, the dewatering profile of fluid leaving the

basket, and the axial pressure profile. Associated with these variables is the output solid volume fraction ϕ_{out}, and the location within the press $\hat{z} = \hat{z}_T$ at which the transition to shunting occurs, where $\hat{z}$ is the axial distance along the press.

Within the constant-pressure churning zone, the solid material is well-mixed radially and the total load on the material is given by the feed pressure p_{in}. Since fluid is lost through the permeable basket along the churning zone, the solid volume fraction ϕ increases from the initial feed value ϕ_{in} until the transition point $\hat{z} = \hat{z}_T$, where the balance of the mean network stress (discussed in detail in §2.2) with the inlet pressure dictates the solid volume fraction.

The location of the transition point $\hat{z}_T$ is determined via the pressure condition at the end of the press. We consider presses with an obstructing cone to provide the counter pressure at the outlet p_{out}; this must be balanced by the mean network stress acting on the basket at the end of the press. The model equations for the shunting zone, which we develop below, may be solved starting from any transition point location $\hat{z}_T$ up to the end of the press to yield a particular value of the mean network stress there. Only one transition point location will lead to a match of that stress with the outlet pressure p_{out}, however, and so an iteration procedure must used to find the correct $\hat{z}_T$ (*cf.* [8]).

In developing the model equations for the shunting zone, we make use of typical geometrical parameters for a screw press to simplify the full equations of motion. For the Thule SP23 screw press shown in figure 1, for example, the screw is approximately 1.5 m long and is housed within a 23 cm diameter cylindrical basket. As one winds along the helical conduit of this press, the convergence of the flight and the expansion of the shaft are both relatively slow: the flight's pitch decreases from an initial value of 25 cm to approximately 9 cm at the end of the press, which represents a decrease of approximately 0.3 cm per radian of turn, and the shaft expands in radius by approximately 3.8 cm per meter length of press.

2.2 Equations of motion in the shunting zone

To model the shunting zone, we assume that the solid is able to resist deformation through an effective solid network stress following Terzaghi [18], and the fluid flow can be described by Darcy's law. The solid and fluid phases are both treated as continua, and the solid volume fraction is ϕ. The fluxes of both the solid and liquid phases are written $\hat{\mathbf{u}}_s$ and $\hat{\mathbf{u}}_f$, respectively, where the hat decoration denotes dimensional variables. We neglect any inertial effects: the compaction due to the contracting geometry is relatively slow, with a pore-scale Reynolds number for the wood pulp pressing of [12] of around 10^{-4}. We also neglect gravity: the ratio of the buoyancy force to a characteristic measure of the network stress p_* is $(\rho_s - \rho_f)g\hat{r}_b/p_*$, where ρ_s and ρ_f are the densities of the (incompressible) solid and fluid constituents respectively, g is the gravitational acceleration, and $\hat{r}_b$ is the basket radius; for the wood pulp press of [12], this ratio is always less than 0.05, although gravitational effects may be more important for other materials, particularly if the press is unsaturated.

In steady state, mass conservation for each phase, Darcy's law, and stress balance are as follows [19, 20, 13–15]:

$$\hat{\boldsymbol{\nabla}} \cdot (\phi\hat{\mathbf{u}}_s) = 0, \tag{1}$$

$$\hat{\boldsymbol{\nabla}} \cdot [(1-\phi)\hat{\mathbf{u}}_f] = 0, \tag{2}$$

$$(1-\phi)(\hat{\mathbf{u}}_s - \hat{\mathbf{u}}_f) = \frac{k(\phi)}{\mu}\hat{\boldsymbol{\nabla}}\hat{p}, \tag{3}$$

$$\hat{\boldsymbol{\nabla}} \cdot (-\hat{p}\boldsymbol{I} + \hat{\boldsymbol{S}}) = 0, \tag{4}$$

where $k(\phi)$ is the ϕ-dependent permeability of the suspension, μ is the fluid viscosity, $\hat{p}$ is the fluid pore pressure, $\boldsymbol{I}$ is the identity tensor, and the effective solid network stress is $\hat{\boldsymbol{\mathcal{S}}}$. To close this set of equations for the fluxes $\hat{\mathbf{u}}_s$ and $\hat{\mathbf{u}}_f$, pore pressure $\hat{p}$ and solid fraction ϕ, we require a constitutive law for the network stress $\hat{\boldsymbol{\mathcal{S}}}$ and suitable boundary conditions on the confining walls. We must also locate the beginning of the shunting zone according to the stress balances outlined earlier; we delay those considerations until after we complete the reduction of the governing equations, at which point it becomes more straightforward to impose the initiation of shunting.

In consolidation theory, the network stress $\hat{\boldsymbol{\mathcal{S}}}$ is typically modeled *via* a ϕ-dependent isotropic plastic yield pressure, $\hat{\boldsymbol{\mathcal{S}}} = -p_Y(\phi)\boldsymbol{I}$, whenever network deformation occurs ($\hat{\boldsymbol{\nabla}} \cdot \hat{\mathbf{u}}_s \neq 0$); otherwise, the magnitude of $\hat{\boldsymbol{\mathcal{S}}}$ is smaller than $p_Y(\phi)$ [13]. More generally, it is possible for such networks to exhibit rate-dependent behaviour once deformation occurs [19,20], and this extension to the effective network stress was found necessary to describe the behaviour of paper-making fibre suspensions [14,15]. We therefore write $\hat{\boldsymbol{\mathcal{S}}} = \hat{S}\boldsymbol{I}$, with $\hat{S} < 0$ under compression, and set the mean solid network stress to be

$$\hat{S} = \left[\frac{p_Y(\phi)}{|\hat{\boldsymbol{\nabla}} \cdot \hat{\mathbf{u}}_s|} + \hat{\Lambda}(\phi) \right] \hat{\boldsymbol{\nabla}} \cdot \hat{\mathbf{u}}_s, \tag{5}$$

so that $\hat{\Lambda}(\phi)$ is a ϕ-dependent bulk viscosity, which represents a generic form of constitutive behaviour of two-phase solid-liquid materials after linearisation in the solid compression rate [19] (see [21] for a more elaborate constitutive relation for paper-making fibre suspensions which is nonlinear in the compression rate). The compressive yield stress $p_Y(\phi)$ is typically measured experimentally. For cellulose fibre suspensions, some success has been achieved by prescribing $\hat{\Lambda}(\phi) = \eta\phi^2$, where η is a material parameter [14,15]. So that the analysis of the model remains as general as possible, we shall derive the model for the general constitutive relation (5) before considering the model predictions for limiting behaviour of the constitutive relation for materials with and without a solid bulk viscosity. For direct comparison to experimental data, we shall then restrict the constitutive relation to those appropriate for the particular cases of paper-making fibre suspension pressing [12] and clay pressing [11].

On solid surfaces with normal vector $\mathbf{n}$ we apply the no-penetration boundary condition $\mathbf{n} \cdot \hat{\mathbf{u}}_s = \mathbf{n} \cdot \hat{\mathbf{u}}_f = 0$ on both the solid and fluid phases. For a permeable surface, we impose $\mathbf{n} \cdot \hat{\mathbf{u}}_s = 0$ on the solid phase, and assume there is no resistance to fluid flow, so that $\hat{p} = 0$ (neglecting atmospheric pressure).

2.3 Local coordinate system

We now work in the frame of the shaft and helical flight, and let $(\hat{x}, \hat{y}, \hat{z})$ and $(\hat{r}, \theta, \hat{z})$ denote global Cartesian and polar coordinates, where $\hat{z}$ is directed along the axis of the press. The flight meets the basket along a helical path parameterised by $0 \leq s \leq 2N\pi$, where $N \gg 1$ is the number of turns of the screw (see Figure 1a). In the polar coordinates this path reads

$$\hat{r} = r_b, \quad \theta = s, \quad \hat{z} = \hat{\beta}(s) \equiv \frac{\hat{l}}{2\pi}[s - f(s)], \tag{6}$$

where r_b is the (constant) radius of the basket, $\hat{l}$ is the initial pitch of the flight, and the function $f(s)$ describes how the flight converges as one progresses down the press. Without any convergence of the flight, *i.e.* constant pitch, we would have $f(s) = 0$ and $\hat{\beta}(s) = \hat{l}s/2\pi$ (so that after

one turn of the flight, s increases by 2π, and $\hat{\beta}$, or $\hat{z}$, increases by $\hat{l}$). In the Cartesian coordinates the path is

$$\hat{x} = r_b \cos s, \quad \hat{y} = r_b \sin s, \quad \hat{z} = \hat{\beta}(s). \tag{7}$$

We now introduce a local non-orthogonal coordinate system $(\hat{r}, \varphi, \hat{\xi})$ based on the meeting point between the flight and the basket (see Figure 1b). We define the coordinates as follows:

$$\hat{r} = \hat{r}, \quad \varphi = \theta, \quad \hat{\xi} = \hat{z} - \hat{\beta}(\varphi), \tag{8}$$

so that $\hat{r}$ remains the radial distance from the centreline, the angle φ parameterises the turn along the helical path of the flight and is everywhere tangent to the flight, and $\hat{\xi}$ measures the axial distance from the flight at position φ. The domain for $(\hat{r}, \varphi, \hat{\xi})$ is

$$\hat{r}_w(\hat{\xi} + \hat{\beta}(\varphi)) < \hat{r} < r_b, \quad 0 < \varphi < 2N\pi, \quad 0 < \hat{\xi} < \hat{l}(1 - b(\varphi)), \tag{9}$$

where $b(\varphi) = [f(\varphi + 2\pi) - f(\varphi)]/2\pi$ and $\hat{r}_w(\hat{z})$ is the (slowly varying) radius of the inner shaft at position $\hat{z}$ along the press (see Figure 1b,c). Note that the domain for $\hat{\xi}$ assumes that the wall of the flight is infinitesimally thin. The local and Cartesian coordinates are related by

$$\hat{x} = \hat{r} \cos \varphi, \quad \hat{y} = \hat{r} \sin \varphi, \quad \hat{z} = \hat{\xi} + \hat{\beta}(\varphi). \tag{10}$$

2.4 The shunting zone in the helical frame

In terms of the local $(\hat{r}, \varphi, \hat{\xi})$ coordinate system (see appendix A), we set $\hat{\mathbf{u}}_{f,s} = (\hat{u}_{f,s}, \hat{v}_{f,s}, \hat{w}_{f,s})$ and write the equations of motion as

$$\frac{1}{\hat{r}} \frac{\partial}{\partial \hat{r}} (\hat{r} \phi \hat{u}_s) + \frac{\partial}{\partial \varphi} \left(\frac{\phi \hat{v}_s}{A} \right) + \frac{\partial}{\partial \hat{\xi}} (\phi \hat{w}_s) = 0, \tag{11}$$

$$\frac{1}{\hat{r}} \frac{\partial}{\partial \hat{r}} [\hat{r}(1 - \phi)\hat{u}_f] + \frac{\partial}{\partial \varphi} \left(\frac{(1 - \phi)\hat{v}_f}{A} \right) + \frac{\partial}{\partial \hat{\xi}} [(1 - \phi)\hat{w}_f] = 0, \tag{12}$$

$$(1 - \phi)(\hat{u}_s - \hat{u}_f) = \frac{k(\phi)}{\mu} \frac{\partial \hat{p}}{\partial \hat{r}}, \tag{13}$$

$$(1 - \phi)(\hat{v}_s - \hat{v}_f) = \frac{Ak(\phi)}{\hat{r}^2 \mu} \left[\frac{\partial \hat{p}}{\partial \varphi} - \hat{\beta}' \frac{\partial \hat{p}}{\partial \hat{\xi}} \right], \tag{14}$$

$$(1 - \phi)(\hat{w}_s - \hat{w}_f) = \frac{k(\phi)}{\hat{r}^2 \mu} \left[A^2 \frac{\partial \hat{p}}{\partial \hat{\xi}} - \hat{\beta}' \frac{\partial \hat{p}}{\partial \varphi} \right], \tag{15}$$

$$\frac{\partial}{\partial \hat{r}} \left(-\hat{p} + \hat{S} \right) + \frac{(\hat{\beta}')^2}{\hat{r} A^2} \left(-\hat{p} + \hat{S} \right) = 0, \tag{16}$$

$$\frac{\partial}{\partial \varphi} \left(\frac{-\hat{p} + \hat{S}}{A^2} \right) = 0, \tag{17}$$

$$\frac{\partial}{\partial \hat{\xi}} \left(-\hat{p} + \hat{S} \right) + \frac{\hat{\beta}''}{A^2} \left(-\hat{p} + \hat{S} \right) = 0, \tag{18}$$

where $A(\hat{r}, \varphi) = \sqrt{\hat{r}^2 + \hat{\beta}'^2}$ is the scale-factor for the φ-direction and the primes denote differentiation with respect to φ.

The boundary conditions on the normal components of velocity on the flight, inner shaft, and basket are as follows: first, the left-side flight surface $\hat{\xi} = 0$ has normal vector

$$\mathbf{n} = -\frac{A\hat{\beta}'}{\hat{r}^2}\hat{\mathbf{e}}_\varphi + \frac{A^2}{\hat{r}^2}\hat{\mathbf{e}}_\xi,\tag{19}$$

where $\hat{\mathbf{e}}_\varphi$ and $\hat{\mathbf{e}}_\xi$ are the (mutually non-orthogonal) unit vectors in the φ and $\hat{\xi}$ directions respectively. The condition of no penetration gives

$$\hat{w}_s = \hat{w}_f = 0 \text{ at } \hat{\xi} = 0.\tag{20}$$

Next, the right-side flight surface $\hat{\xi} = \hat{l}(1 - b(\varphi))$ has normal vector

$$\mathbf{n} = \frac{A}{\hat{r}^2}(\hat{l}b' - \hat{\beta}')\hat{\mathbf{e}}_\varphi + \frac{1}{\hat{r}^2}(A^2 - \hat{\beta}'\hat{l}b')\hat{\mathbf{e}}_\xi,\tag{21}$$

and no penetration gives

$$\hat{w}_{s,f} = -\frac{\hat{l}b'}{A}\hat{v}_{s,f} \text{ at } \hat{\xi} = \hat{l}(1 - b(\varphi)).\tag{22}$$

The shaft surface $\hat{r} = \hat{r}_w(\hat{\xi} + \hat{\beta}(\varphi))$ has normal vector

$$\mathbf{n} = \hat{\mathbf{e}}_r - \hat{r}'_w\hat{\mathbf{e}}_\xi,\tag{23}$$

where $\hat{\mathbf{e}}_r$ is the unit vector in the $\hat{r}$ direction. With no penetration we find that

$$\hat{u}_{s,f} = \hat{r}'_w\hat{w}_{s,f} + \frac{\hat{r}'_w\hat{\beta}'}{A}\hat{v}_{s,f} \text{ at } \hat{r} = \hat{r}_w(\hat{\xi} + \hat{\beta}(\varphi)).\tag{24}$$

Finally, on the basket surface $\hat{r} = r_b$ we have

$$\hat{u}_s = 0 \text{ and } \hat{p} = 0.\tag{25}$$

2.5 Nondimensionalisation and reduction

The geometry of a screw press allows us to make a number of simplifying steps in our analysis. In detail, we explore the following asymptotic limit: given that the pitch is slowly varying, so that $f'(s), f''(s) \ll 1$, we may set $\hat{\beta}' \sim \hat{l}/2\pi$ and $\hat{\beta}'' \ll A$, and reduce the local calculus to the case of constant pitch. Next, the basic pitch $\hat{l}$ is typically smaller than the shaft circumference $2\pi\hat{r}_w$, particularly towards the end of the press, and so we therefore assume that $\hat{l} \ll 2\pi\hat{r}_w$. This allows us to neglect all terms containing $\hat{\beta}'/\hat{r}$ except in the boundary conditions, and to set $A \sim \hat{r}$. We see that the combined effect of these two approximations is to reduce the calculus associated with the local coordinates to that of (local) cylindrical polar coordinates. Finally, the radius $\hat{r}_w(\hat{z})$ is slowly varying, so that $\hat{r}_w(\hat{\xi} + \hat{\beta}(\varphi)) \sim \hat{r}_w(\hat{\beta}(\varphi))$, and so locally at each φ the shaft is approximately parallel to the basket. These asymptotic approximations are consistent with the geometry of both the press shown in figure 1 and detailed further in Appendix B.1, and the press used by Shirato *et al.* [11], which is detailed in Appendix B.2.

To nondimensionalise the equations of motion, we scale lengths with the constant basket radius r_b, pressures and stresses by a characteristic pressure of the medium $p_* = p_Y(\phi_c)$, and permeability with a characteristic scale $k_* = k(\phi_c)$. Here, ϕ_c is a characteristic volume fraction, taken to be $\phi_c = 0.1$ as a typical value for the cellulose fibre suspensions. To scale the velocity components, we note that for pure axial shunting, the φ component of velocity is given by solid-body rotation in the frame of the shaft and flight. We therefore scale $\hat{v}_{s,f}$ with Ωr_b, where Ω is

the rotation rate of the shaft. The remaining two velocity components must scale with the rate of contraction of the local geometry due to the expanding shaft or converging flight. Denoting the typical rate of change of the channel's cross-sectional area per unit distance along the channel by $\hat{\Delta}$, we scale both components with $Q \equiv \Omega\hat{\Delta}$. For example, since the presses we consider here both have an expanding shaft, we may set $\hat{\Delta} = \hat{l}R'_*/2\pi$, where R'_* denotes a typical scale for $\hat{r}'_w$ (so that $\hat{\Delta}$ is a typical scale for $\partial\hat{r}_w/\partial\varphi \sim \hat{r}'_w\beta'(\varphi)$). In summary, we set

$$\hat{v}_{s,f} = \Omega r_b v_{s,f}, \quad (\hat{u}_{s,f}, \hat{w}_{r,s}) = Q(u_{s,f}, w_{s,f}), \quad \hat{r} = r_b r, \quad \hat{\xi} = r_b\xi, \quad \hat{z} = r_b z,$$
$$\hat{\beta} = r_b\beta, \quad \hat{r}_w = r_b r_w, \quad \hat{l} = r_b l, \quad \hat{S} = -p_* P, \quad k = k_* K. \tag{26}$$

For a press with $N \gg 1$ turns of the flight, the length of the press is $L = \hat{l}[2N\pi - f(2N\pi)]/2\pi \sim N\hat{l} \gg \hat{l}$. We therefore observe that the rotational coordinate φ is relatively long, and so we make the change of variable $\varphi = \delta^{-1}q$, where $\delta = \hat{\Delta}/r_b \ll 1$. The new variable q therefore takes values in the range $0 \le q \le q_{out} \equiv 2\pi N\delta$. For the press in Figure 1, $\delta = 0.014$ and $q_{out} \approx 0.7$ ($\varphi_{out} = 2\pi N \approx 50$), whereas $\delta = 2.3 \times 10^{-4}$ and $q_{out} \approx 0.03$ ($\varphi_{out} = 2\pi N \approx 138$) for the press of Shirato *et al.* [11].

To leading order in δ, equations (16) and (18) now indicate that the total stress $-p + P$ is independent of r and ξ, while the remaining stress equation (17), which indicates that $-p + P$ varies slowly with φ, becomes redundant in this limit, being decoupled from the the remaining equations of motion (11–15). These can be reduced at leading order to

$$\frac{1}{r}\frac{\partial}{\partial r}(r\phi u_s) + \frac{1}{r}\frac{\partial}{\partial q}(\phi v_s) + \frac{\partial}{\partial\xi}(\phi w_s) = 0, \tag{27}$$

$$\frac{1}{r}\frac{\partial}{\partial r}[r(1-\phi)u_f] + \frac{1}{r}\frac{\partial}{\partial q}[(1-\phi)v_f] + \frac{\partial}{\partial\xi}[(1-\phi)w_f] = 0, \tag{28}$$

$$(1-\phi)(u_s - u_f) = -\gamma K(\phi)\frac{\partial P}{\partial r}, \tag{29}$$

$$(1-\phi)(v_s - v_f) = 0, \tag{30}$$

$$(1-\phi)(w_s - w_f) = -\gamma K(\phi)\frac{\partial P}{\partial\xi}, \tag{31}$$

where the dimensionless parameter,

$$\gamma = \frac{k_* p_*}{Q\mu r_b} \equiv \frac{k_* p_*}{\Omega\hat{\Delta}\mu r_b} \tag{32}$$

quantifies the rate of compaction in relation to the diffusion of effective solid network stress.

In view of (30), Darcy's law demands that there can be little slip between phases in the φ direction, so that $v_s \approx v_f$. Moreover, as argued in §2.1, axial transport in the shunting zone implies $\hat{v}_s = \hat{v}_f = \Omega\hat{r}$ in the frame of the basket, or $v_s = v_f = r$. Hence, (27)–(31) become

$$\frac{\partial\phi}{\partial q} + \frac{1}{r}\frac{\partial}{\partial r}(r\phi u_s) + \frac{\partial}{\partial\xi}(\phi w_s) = 0, \tag{33}$$

$$-\frac{\partial\phi}{\partial q} + \frac{1}{r}\frac{\partial}{\partial r}[r(1-\phi)u_s] + \frac{\partial}{\partial\xi}[(1-\phi)w_s] = 0, \tag{34}$$

$$(1-\phi)(u_s - u_f) = -\gamma K(\phi)\frac{\partial P}{\partial r}, \tag{35}$$

$$(1-\phi)(w_s - w_f) = -\gamma K(\phi)\frac{\partial P}{\partial\xi}, \tag{36}$$

where we have reordered the terms in the continuity equations to emphasise how q (and hence φ) now plays a similar role to time in an equivalent pressure filtration problem. The dimensionless boundary conditions at leading order are

$$w_s = w_f = 0 \ \text{ at } \xi = 0, \tag{37}$$

$$w_s = w_f = -l\dot{b} \ \text{ at } \xi = l(1 - b(q)), \tag{38}$$

$$u_s = u_f = \dot{r}_w \ \text{ at } r = r_w(\beta(q)), \tag{39}$$

$$u_s = 0 \ \text{ and } p = 0 \ \text{ at } r = 1, \tag{40}$$

where the dots on b and r_w denote differentiation with respect to q.

The asymptotic reductions thus far are based on the geometry of the press. To complete the reduction of the model, we note that (33–40) admit a solution in which the material remains uniform in the local coordinate ξ between consecutive walls of the flight (see figure 1(c)); *i.e.* that $\partial P/\partial \xi = \partial \phi/\partial \xi = \partial u_{s,f}/\partial \xi = 0$. If we therefore assume that this is the case, then Darcy's law in the ξ-direction implies that $w_s = w_f$, and the continuity equations and boundary conditions (37–38) now furnish

$$w_s = w_f = -\frac{\dot{b}\xi}{(1 - b)}.$$

We substitute this expression into the two continuity equations and add them to find

$$\frac{1}{r}\frac{\partial}{\partial r}[r(\phi u_s + (1 - \phi)u_f)] = \frac{\dot{b}}{(1 - b)}. \tag{41}$$

The integral of this equation with respect to r and application of the boundary conditions (39) now gives

$$(1 - \phi)(u_s - u_f) = u_s - \left(\frac{r^2 - r_w^2}{2r}\right)\left(\frac{\dot{b}}{1 - b}\right) - \dot{r}_w\frac{r_w}{r}, \tag{42}$$

which may be substituted into (35).

2.6 Model summary

To summarize, we split the press into two zones, an initial churning zone followed by a shunting zone. The model inputs are the inlet pressure p_{in}, outlet pressure p_{out} and the rotation rate Ω of the flight-shaft assembly, which after non-dimensionalisation are encoded in $P_{in} \equiv p_{in}/p_*$, $P_{out} \equiv p_{out}/p_*$, and $\gamma \propto \Omega^{-1}$, respectively. The solid flux through the machine and the transition point between the two zones are output variables. The shunting zone is described by

$$\frac{\partial \phi}{\partial q} + \frac{1}{r}\frac{\partial}{\partial r}(r\phi u) - \frac{\dot{b}}{1 - b}\phi = 0, \tag{43}$$

$$u = \left(\frac{r^2 - r_w^2}{2r}\right)\left(\frac{\dot{b}}{1 - b}\right) + \dot{r}_w\frac{r_w}{r} - \gamma K(\phi)\frac{\partial P}{\partial r}, \tag{44}$$

subject to the boundary conditions,

$$u(r_w, q) = \dot{r}_w(q) \qquad \text{and} \qquad u(1, q) = 0, \tag{45}$$

where we have eased the notation by setting $u(r, q) = u_s$. The dimensionless rheology is given by

$$P = -\left[\frac{\Pi_Y(\phi)}{|\boldsymbol{\nabla} \cdot \mathbf{u}_s|} + \frac{\epsilon}{\gamma}\Lambda(\phi)\right]\boldsymbol{\nabla} \cdot \mathbf{u}_s, \qquad \boldsymbol{\nabla} \cdot \mathbf{u}_s = \frac{1}{r}\frac{\partial}{\partial r}(ru) - \frac{\dot{b}}{1-b}, \qquad (46)$$

where $p_Y(\phi) = p_* \Pi_Y(\phi)$, $\hat{\Lambda}(\phi) = \eta\Lambda(\phi)$, and the parameter ϵ is given by

$$\epsilon = \frac{\eta k_*}{\mu r_b^2}, \qquad (47)$$

which quantifies the relative importance of the rate-dependent part of the stress.

The final model equations combine a second-order-in-r equation (44) for u, solved subject to the two boundary conditions (45), with an advection equation (43) for ϕ. The latter must be initialised by noting that the shunting zone begins at the transition point, $z = z_T \equiv \beta(\varphi_T)$, or $q = q_T$, at which location the solid stress balances the pressure of the churning zone to establish the local solid volume fraction ϕ_T. That is, $P = P_{in}$ and $\phi = \phi_T$ at $q = q_T$.[1] However, q_T is not yet known, and must be determined by demanding that the material load against the basket (where the fluid pore pressure vanishes) balance the counter pressure provided by the cone at the end of the press: $P_{out} = P(1, q_{out})$. We therefore integrate the equations of motion (43–44) for the shunting zone from a trial transition point $q = q_T$ up to the end of the press $q = q_{out}$. The starting point q_T is adjusted using a bisection algorithm until $P(1, q_{out}) = P_{out}$; that is, the network stress on the basket at $q = q_{out}$ found from integrating (43–44) matches the outlet pressure P_{out}. Having found the transition point in this fashion, the dimensionless solid flux through the press is given by $Q_s = \phi_T \mathcal{A}(q_T)$, where $\mathcal{A}(q) = l(1-b)(1-r_w^2)/2$ is the dimensionless cross-sectional area of the helical channel (*i.e.* the volume per radian of the section shown in figure 1(c)), corresponding to a dimensional flux of

$$\hat{Q}_s \equiv r_b^3 \Omega Q_s = r_b^3 \Omega \phi_T \mathcal{A}(q_T). \qquad (48)$$

Although the solid flux is conserved along the press, the fluid flux is not, since water may leave the press across the permeable basket. The dimensionless fluid flux is $Q_f = (1 - \overline{\phi})\mathcal{A}(q)$, where $\overline{\phi}$ is the mean solid volume fraction at location q.

The model encodes the geometrical constriction of the press *via* the functions $b(q)$ and $r_w(q)$. The constitutive behaviour of the material being pressed is contained in the functions $\Pi_Y(\phi)$ and $k(\phi)$; if the material has a bulk viscosity then its solid fraction-dependence is given by $\Lambda(\phi)$ and its magnitude is quantified through ϵ. The rotation rate of the press, Ω, enters through the dimensionless compaction time γ and is one of the three operating parameters we consider. All of these variables have analogues in models of filtration [14] or flow-induced compaction [15], although there is novelty in the bi-axial nature of the geometrical constriction (see Appendix C). In addition, the dimensionless duration of the compaction, q_{out}, cannot be scaled to unity, as in those models; instead, this duration varies with the number of turns of the flight and is implicitly linked to the press geometry. The remaining two operating parameters are p_{in} and p_{out}, which are transformed into their dimensionless counterparts P_{in} and P_{out} using a characteristic material strength. These parameters have no analogue in pressure filtration or flow-induced compaction, but are key in setting the transition point between churning and shunting.

---

[1] Note that if the solid stress is rate dependent ($\Lambda \neq 0$ in (46)), then ϕ_T is not immediately prescribed by P_{in}, but also depends on the local strain rate at the transition point q_T (requiring us to solve (44) and (46) with $P = P_{in}$ for both $\phi = \phi_T$ and $u(r, q_T)$).

3 Interrogating the model

3.1 Sample solutions

Given the large number of parameters remaining in the model, in order to present some sample solutions we first restrict attention to a single press (shown in figure 1 and detailed in Appendix B.1) and a single material, namely a softwood cellulose fibre suspension (NBSK). The compressive yield stress $p_Y(\phi)$ and permeability $k(\phi)$ for this material have been calibrated experimentally via the procedure outlined by Hewitt *et al.* [14] (see Appendix B.1). In their filtration studies, Hewitt *et al.* [14] observed the necessity of including a rate-dependent stress in the two-phase model to accurately capture the observed dynamics. The functional form $\hat{\Lambda}(\phi) = \eta\phi^2$ with $\eta = 10^7$ Pa s was found to be suitable for NBSK; we continue with this prescription here.

Having restricted the model to this press and material, we are left with the three operating parameters P_{in}, P_{out}, and γ. Figure 2 shows sample model predictions, with values adopted for these operating parameters that correspond to typical values used in the pilot plant trials conducted in [12]. The sample solutions have transition points q_T arising near the inlet, midsection or end of the press. As designed in the formulation of the model, the pressure is uniform over the churning zone, then increases abruptly towards the end of the press as material is consolidated over the shunting zone. Likewise, the flux of water leaving through the basket at each axial position is dictated by the press geometry over the shunting section. The profiles of solid volume fraction ϕ illustrate how, in all three cases, the material differentially compacts against the basket and reaches the end of the press with substantial radial gradients; for the case with leftmost transition point, the shunting zone is the longest, resulting in the greatest differential compaction.

In the model, the characteristic time for compaction is controlled by the parameter γ, which is relatively small for the examples in figure 2 and promotes the formation of radial gradients in ϕ. On the other hand, the rate-dependent stress, whose effect is gauged by ϵ, acts to smooth out any such gradients; adopting large values for ϵ renders the material completely uniform in r. The sample solutions of figure 2 have $\epsilon = 1.11$, and represent an intermediate behaviour in which the compaction against the basket competes with the smoothing action of the rate-dependent stress. Note that, for pulp at low values of γ, the adopted forms for $p_Y(\phi)$ and $k(\phi)$ promote the establishment of boundary layers under compaction unless the rate-dependent stress exerts sufficient smoothing [14].

3.2 Nearly uniform, slow consolidation

In the limit $\gamma \gg 1$, the model can be simplified further and solved analytically (*cf.* [13,14]) to establish precisely how the transition point becomes located. The key point is that, in such relatively slow consolidation, the solid volume fraction remains roughly uniform in r. As a consequence, (43) reduces to

$$\frac{1}{r}\frac{\partial}{\partial r}(ru) \approx \frac{\dot{b}}{1-b} - \frac{\dot{\phi}}{\phi}. \tag{49}$$

Conservation of the solid across each cross-section also implies that

$$\phi_T \mathcal{A}_T = \int_0^{1-b} \int_{r_w}^1 \phi\, r \mathrm{d}r \mathrm{d}\xi, \tag{50}$$
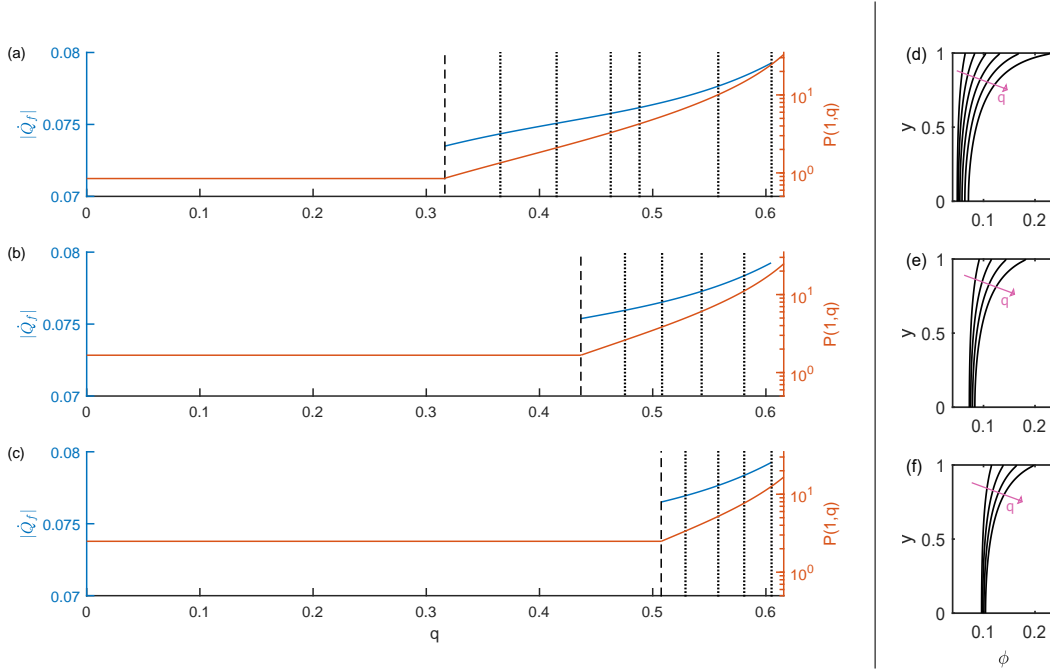
Fig. 2 Sample model predictions for NBSK pulp. (a,d) with $(P_{in}, P_{out}, \gamma) = (0.85, 33.2, 0.027)$, (b,e) with $(P_{in}, P_{out}, \gamma) = (1.67, 24.9, 0.036)$ and (c,f) with $(P_{in}, P_{out}, \gamma) = (2.49, 16.6, 0.056)$. In all cases, $\epsilon = 1.11$. The plots in (a-c) show the dimensionless dewatering fluid flux $|\dot{Q}_f|$ (blue curves; left-hand axis) and the dimensionless effective stress $P(r = 1, q)$ (red curves; right-hand axis) against q. The transition points are shown by a vertical black dashed line. (d-f) show model profiles of ϕ against $y \equiv 1 + (r - 1)/(1 - r_w(q))$ at the axial locations shown by dotted lines in (a-c).

where $\mathcal{A}_T = \mathcal{A}(q_T)$, and so under the uniform ϕ approximation, $\phi_T \mathcal{A}_T \approx \phi \mathcal{A}$. Thus,

$$u \approx \left(\frac{\dot{b}}{1-b} + \frac{\dot{\mathcal{A}}}{\mathcal{A}} \right) \frac{(r^2 - r_w^2)}{2r} + \frac{r_w}{r} \dot{r}_w. \tag{51}$$

Darcy's law (44) now implies that

$$\frac{\dot{\mathcal{A}}}{\mathcal{A}} \frac{(r^2 - r_w^2)}{2r} \approx -\gamma K(\phi) \frac{\partial P}{\partial r}, \tag{52}$$
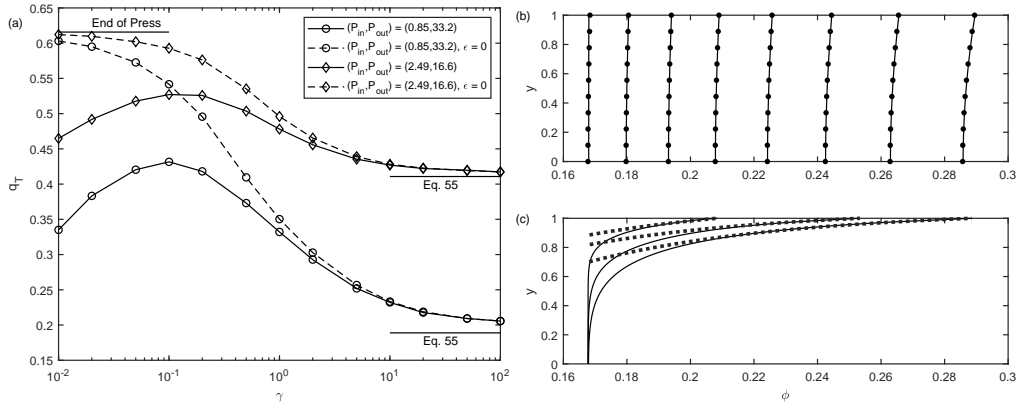
whereas the constitutive law gives

$$P \approx \Pi_Y(\phi) - \frac{\epsilon}{\gamma} \Lambda(\phi) \frac{\dot{\mathcal{A}}}{\mathcal{A}}, \qquad \left(\boldsymbol{\nabla} \cdot \mathbf{u}_s \approx \frac{\dot{\mathcal{A}}}{\mathcal{A}} < 0 \right). \tag{53}$$

Integrating the approximation to Darcy's law (52) leads to

$$B(\phi) \approx B(\phi_w) + \gamma^{-1} \left| \frac{\dot{\mathcal{A}}}{\mathcal{A}} \right| \left[\frac{1}{4}(r^2 - r_w^2) - \frac{1}{2} r_w^2 \log(r/r_w) - \epsilon \int_{\phi_w}^{\phi} K(\Phi) \Lambda(\Phi) \mathrm{d}\Phi \right], \tag{54}$$

where $\phi_w(q) \equiv \phi(r_w, q)$, and

$$B(\phi) = \int K(\Phi) \Pi_Y'(\Phi) \mathrm{d}\Phi, \tag{55}$$

Fig. 3 (a): The transition point q_T as a function of γ for two combinations of P_{in} and P_{out} and for NBSK with (solid) or without (dashed) a solid bulk viscosity ($\epsilon = \Lambda(\phi) = 0$) in the press in [12]. (b): Solid fraction profiles during consolidation of NBSK pulp for $(P_{in}, P_{out}, \gamma) = (2.49, 16.6, 50)$ (solid) along with solutions to (54) (dots) at $q = 0.42, 0.45, 0.47, 0.50, 0.52, 0.55, 0.58$ and 0.60. (c): Solid fraction profiles during consolidation of NBSK pulp setting $\epsilon = \Lambda(\phi) = 0$ for $(P_{in}, P_{out}, \gamma) = (2.49, 16.6, 0.2)$ (solid) along with solutions to (58) in the boundary layer (dots) using the numerical value of ϕ_1 at $q = 0.58, 0.60$ and 0.61.

which is related to the solid stress diffusivity $D(\phi)$ of [13,14] via $B'(\phi) = D(\phi)/\phi$.

Given the implicit solution for the solid fraction implied by (54), the mass conservation constraint (50) can now be employed to determine ϕ_w, and hence the $O(\gamma^{-1})$ correction to $\phi \approx \phi_T \mathcal{A}_T/\mathcal{A}$. Working only to leading order, however, we observe that

$$\Pi_Y(\phi_T) = P_{in} \text{ and } \Pi_Y(\phi_{out}) \approx \Pi_Y\left(\frac{\phi_T \mathcal{A}_T}{\mathcal{A}_{out}}\right) \approx P_{out}, \quad \text{or} \quad \mathcal{A}_T \approx \mathcal{A}_{out}\frac{\Pi_Y^{-1}(P_{out})}{\Pi_Y^{-1}(P_{in})}, \quad (56)$$

where ϕ_{out} and $\mathcal{A}_{out}$ denote the final solid fraction and cross-sectional area. This simple result highlights the manner in which the end pressures set the position (or more directly the cross-sectional area) and solid fraction at the transition point, independently of γ.

The improved approximation from (54) is compared with a numerical solution in figure 3(b), using the press in [12] and an NBSK suspension, but this time for $\gamma = 100$. The computed transition point, $q_T \approx 0.417$, agrees satisfyingly with the prediction of $q_T \approx 0.411$ from (56), and the figure demonstrates that the computed solid fraction profiles at various positions along the press compare well with (54). As γ is increased, we see in figure 3(a) that the transition point approaches the predictions provided by (56).

We note, however, that the solution in (54) can potentially fail owing to the precise form of $B(\phi)$ for the NBSK suspension (see figure 10(a,b) and appendix C.3 for an example of such a failure). In particular, for this material, $B(\phi)$ reaches a maximum value just below 8.5 at the largest solid fractions, but right-hand side of (54), increases beyond that limit because of the rising compression factor $|\dot{\mathcal{A}}/\mathcal{A}|$.

The form of $B(\phi)$ for NBSK is characteristic of a material for which the solid stress diffusivity $D(\phi)$ is a decreasing function of ϕ. Other materials, such as the suspension of nylon fibres studied in [14], have the opposite property for $D(\phi)$ (which is connected to whether or not the pore space remains open to fluid flow as maximum packing is approached). With an increasing solid stress diffusivity, the function $B(\phi)$ diverges as ϕ approaches maximum packing, and so it always remains possible to satisfy (54).

3.3 Rapid consolidation in the small bulk viscosity limit

If, instead, the press operates in the limit of rapid consolidation ($\gamma \ll 1$) and the solid bulk viscosity remains small ($\epsilon \ll \gamma$), substantial differential compaction occurs against the basket over the shunting zone (*cf.* [14]). In particular, a boundary layer forms at $r = 1$ with $\phi = \phi_T \equiv \Pi_Y^{-1}(P_{in})$ underneath. The enhanced radial gradients over the boundary layer demand $\partial(r\phi u)/\partial r \approx 0$ from (43), or $\phi u \approx 0$ in view of the second condition in (45). Hence, from (44) and neglecting the solid bulk viscosity,

$$\frac{\gamma D(\phi)}{\phi}\frac{\partial \phi}{\partial r} \approx \frac{1}{2}(1 - r_w^2)\frac{\dot{b}}{1 - b} + r_w \dot{r}_w \equiv \frac{|\dot{\mathcal{A}}|}{l(1 - b)}, \tag{57}$$

which furnishes an implicit expression for the radial distribution of the solid fraction,

$$B(\phi) \approx B(\phi_1) - \frac{|\dot{\mathcal{A}}|(1 - r)}{\gamma l(1 - b)}, \tag{58}$$

given the value at $r = 1$, $\phi_1(q) = \phi(1, q)$, where $B(\phi)$ is again given by (55). To find the solid fraction at the basket, we note that

$$l(1 - b)\int_{r_w}^{1}(\phi - \phi_T)r\mathrm{d}r = (\mathcal{A}_T - \mathcal{A})\phi_T. \tag{59}$$

But

$$\int_{r_w}^{1}(\phi - \phi_T)r\mathrm{d}r \approx \frac{\gamma l(1 - b)}{|\dot{\mathcal{A}}|}\int_{\phi_T}^{\phi_1}(\phi - \phi_T)D(\phi)\frac{\mathrm{d}\phi}{\phi} \tag{60}$$

from (57). Thus,

$$\frac{(\mathcal{A}_T - \mathcal{A})\phi_T|\dot{\mathcal{A}}|}{\gamma l^2(1 - b)^2} \approx \int_{\phi_T}^{\phi_1}(\phi - \phi_T)D(\phi)\frac{\mathrm{d}\phi}{\phi}, \tag{61}$$

which implicitly determines the solid fraction at the basket at the end of the press, $\phi_1(q_{out})$, on setting $q = q_{out}$. The transition point must be then chosen to ensure that $\Pi_Y(\phi_1(q_{out})) = P_{out}$.

It is clear from (61) that a decrease in γ corresponds to an enhancement in the degree of differential compaction, which in turn implies that the pressure must build up from P_{in} to P_{out} over shorter distances. Thus, in this limit of relatively rapid compaction without significant solid bulk viscosity, the transition point q_T must inevitably become dependent on γ and move towards the outlet of the press as the rotation rate is increased, at least until the transition point is close enough to the press outlet for the geometrical conditions inherent in the asymptotic model to break down.

Figure 3(c) shows solid fraction profiles for NBSK pulp in the press in [12], artificially setting $\epsilon = \Lambda(\phi) = 0$, at various locations in the shunting zone for $\gamma = 0.2$. The material differentially compacts against the permeable basket, and the boundary layer structure that forms is well captured by the overlain solutions to (58), using the numerical values of ϕ_1. We see in figure 3(a) that the transition point does indeed monotonically move towards the end of the press as γ is reduced for this artificial NBSK suspension. Unfortunately, we are unable to use (61) to provide an estimate for q_T using the press in [12] because for this press the area contraction rate $\dot{\mathcal{A}}$ is not continuous (near the end of the press, the shaft suddenly stops expanding). At locations where $\dot{\mathcal{A}}$ has a discontinuity, we can no longer neglect q-derivatives in the equations of motion, and so the estimates in (58) and (61) may only be applied in a neighbourhood of the transition point.

3.4 Large solid viscosity

Analytical progress is also possible in the limit of relatively large solid bulk viscosity ($\gamma \ll \epsilon$), for which the rate-dependent stress dominates over the compressive yield stress $\Pi_Y(\phi)$ and radial gradients of the solid fraction are suppressed. The latter guides us to adopt the approximation

$$-\boldsymbol{\nabla} \cdot \mathbf{u} \sim \mathcal{F}(q_T) \equiv \left| \frac{\dot{\mathcal{A}}}{\mathcal{A}} \right|$$

from §3.2, where the local compression rate $\mathcal{F}(q)$ is a function only of the local geometry. The pressure condition at the transition point q_T then reads

$$P_{in} \sim \frac{\epsilon}{\gamma} \Lambda(\phi_T) \mathcal{F}(q_T). \tag{62}$$

The same approximation applied at the outlet implies

$$P_{out} \sim \frac{\epsilon}{\gamma} \Lambda(\phi_{out}) \mathcal{F}(q_{out}). \tag{63}$$

We also know that the (unknown) solid flux Q_s is conserved along the press, and so

$$Q_s = \phi_T \mathcal{A}(q_T) = \phi_{out} \mathcal{A}(q_{out}).$$

Combining these relations, we find

$$Q_s \sim \mathcal{A}(q_{out}) \Lambda^{-1} \left(\frac{\gamma P_{out}}{\epsilon \mathcal{F}(q_{out})} \right) \sim \mathcal{A}(q_T) \Lambda^{-1} \left(\frac{\gamma P_{in}}{\epsilon \mathcal{F}(q_T)} \right). \tag{64}$$

For the particular case of a power-law bulk viscosity with $\Lambda(\phi) = \phi^a$, we summarize the preceding arguments in the formulae,

$$\phi_{out} \sim \frac{\mathcal{G}(q_{out})}{\mathcal{A}(q_{out})} \left(\frac{\gamma P_{out}}{\epsilon} \right)^{1/a}, \tag{65}$$

$$\phi_T \sim \frac{\mathcal{G}(q_T)}{\mathcal{A}(q_T)} \left(\frac{\gamma P_{in}}{\epsilon} \right)^{1/a}, \tag{66}$$

$$Q_s \sim \mathcal{G}(q_{out}) \left(\frac{\gamma P_{out}}{\epsilon} \right)^{1/a} \sim \mathcal{G}(q_T) \left(\frac{\gamma P_{in}}{\epsilon} \right)^{1/a}, \tag{67}$$

$$q_T \sim \mathcal{G}^{-1} \left[\mathcal{G}(q_{out}) \left(\frac{P_{out}}{P_{in}} \right)^{1/a} \right], \tag{68}$$

where $\mathcal{G}(q) = \mathcal{A}(q)/\mathcal{F}(q)^{1/a}$ is a decreasing function of q.

Dimensionally, in terms of the operating parameters p_{in}, p_{out}, and Ω, these estimates imply that the outlet solid fraction is $\phi_{out} \propto (p_{out}/\Omega)^{1/a}$, the solid fraction at the transition point is $\phi_T \propto (p_{in}/\Omega)^{1/a}$, the solid flux is $\hat{Q}_s \propto (\Omega^{a-1} p_{in})^{1/a} \propto (\Omega^{a-1} p_{out})^{1/a}$, and the transition point $\hat{z}_T$ depends on $(p_{out}/p_{in})^{1/a}$. Note that these estimates imply that increasing P_{out} increases the solid flux Q_s. However, we cannot indefinitely increase the solid flux by increasing P_{out} because $\mathcal{G}(q) < \mathcal{G}(0)$, and so increasing P_{out} too far moves the transition point to the beginning of the press, at which point the inlet would jam unless P_{in} were increased to compensate. Indeed, the general condition for a solution to (68) to exist is that $P_{out}/P_{in} < [\mathcal{G}(0)/\mathcal{G}(q_{out})]^a \approx 5.96$ for NBSK pulp in the press in [12].

An alternative method to increase the (dimensional) solid flux is to increase the rotation rate (taking $a > 1$). However, this is at the expense of lowering the output solid fraction unless P_{out} is also increased. Moreover, too large an increase in rotation rate prompts the solid volume fraction at the transition point to decrease below that of the inlet. This is inconsistent with the modelling principle that water is lost over the churning section, and must indicate that the global pressure balance breaks down.

A significant solid bulk viscosity features in many of the experiments in which the paper-making fibre press of [12] operates. Model predictions of the transition point q_T and solid flux Q_s for NBSK pulp in this press are shown in figure 4(a,b), for a range of P_{in} and P_{out} typical of the press operation and two values of γ which account for the range of rotation rates Ω employed; both values of γ are relatively small in comparison to $\epsilon = 1.11$. In general we see that the solid flux increases with γ, P_{out}, and P_{in}, and that the transition point moves towards the feed end of the press as the ratio P_{out}/P_{in} increases. Plotting Q_s against $\sqrt{\gamma P_{out}/\epsilon}$ in figure 4(c) and q_T against $\sqrt{P_{out}/P_{in}}$ in figure 4(d) achieves some collapse of the numerical data. This coincides precisely with the predictions in (67)–(68) if $a = 2$, which is the exponent expected for this pulp suspension [14].

However, figure 3(a) shows that even for $\gamma = 10^{-2}$ there is not yet a sufficient separation between γ and $\epsilon = 1.11$ for the transition point to have become independent of γ, and helps to indicate why the collapse in figure 4(d) is only partially successful. For these intermediate values of $\gamma \lesssim \epsilon$, the transition point exhibits a somewhat complicated dependence on γ in figure 3(a).

3.5 Verification against press data

3.5.1 Pulp

Figure 5(a) shows a comparison between the observed and predicted (dimensional) solid flux for the operating conditions reported in [12] for two different cellulose pulps (NBSK and a second, BCTMP, with properties summarized in Appendix B.1). For NBSK, the model overpredicts the solid flux by a relatively small margin. Figure 5(b) shows a comparison between the experimental observations and model predictions for the total dewatering fluid flux leaving the press through the permeable basket *after* the transition point. After the transition point $\hat{z}_T$, the dewatering fluid flux is prescribed by the geometry change; to compare the model to the experimental data, we use the model's predictions for $\hat{z}_T$ and sum the experimental fluid fluxes recorded after this location on the press and compare to the equivalent quantity derived from the model. Prior to the transition point $\hat{z}_T$, the model does not specify the dewatering fluid flux, but does provide the fluid flux along the press at the transition point. Given the inlet fluid flux, we may therefore estimate the water loss over the churning zone. This prediction for the total dewatering fluid flux leaving the press through the permeable basket *before* the transition point is compared to the experimental data in figure 5(c). For both materials, the model slightly overestimates the dewatering flux after the transition point and slightly underestimates this flux before the transition point.

The slight disagreement between the theoretical and experimental solid and water fluxes can be removed by arguing that its source is a breakdown of perfect axial shunting beyond the transition point; if the material over the shunting section does not move purely axially, but also rotates slightly, then the fluxes must be altered. To incorporate this effect into the model, we make the crude approximation that the effective shunting motion down the press is given by a suitable, constant fraction α of the rotation rate, $\alpha\Omega$, with $0 < \alpha < 1$, *i.e.* for every turn of the shaft the pulp rotates by a fractional turn $1 - \alpha$. Including this additional slip-factor
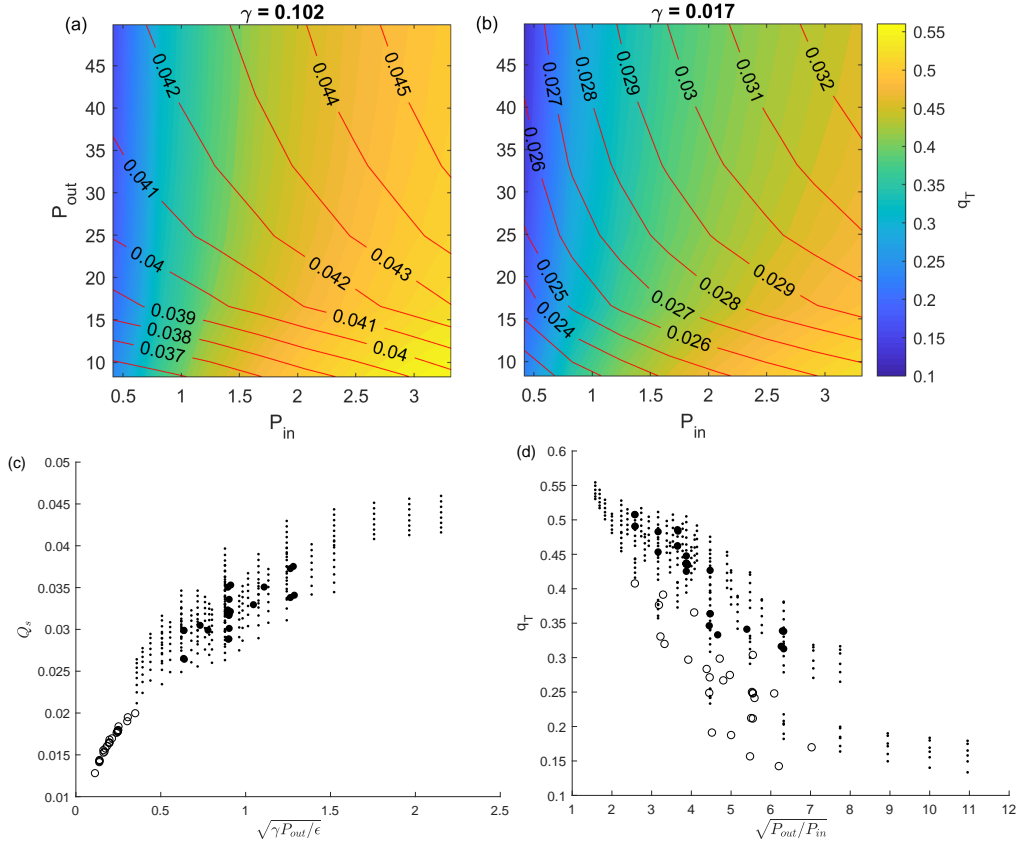
Fig. 4 (a,b): contours of transition point q_T (color) and solid flux Q_s (lines) as a function of inlet pressure P_{in} and outlet pressure P_{out} for (a) $\gamma = 0.102$ and (b) $\gamma = 0.017$ for NBSK pulp in the press in [12]. (c): model prediction for the solid flux plotted against $\sqrt{\gamma P_{out}/\epsilon}$. (d): the full model predictions for the transition point q_T plotted against $\sqrt{P_{out}/P_{in}}$. Large symbols show pilot-plant operating conditions for NBSK (filled) and BCTMP (open) (see §3.5.1). Dots show full model predictions over a wider range of operating conditions for NBSK, for which multiple points at the same abscissa represent variations in P_{in} (c) and γ (d) over the ranges shown in (a,b). Some collapse of the full model solutions in (c,d) is evident, in agreement with the approximations (67–68), given that $a = 2$ for pulp suspensions.

into the model does indeed lower the predicted solid flux for NBSK and preserve the relatively good agreement for BCTMP, with the single choice $\alpha = 0.75$ adequately aligning the theoretical results with most of the data; see figure 5(a). Additionally, the predictions for the dewatering fluid fluxes both before and after the transition point are brought into line with the experimental observations with this same choice of α; see figures 5(b,c). Nevertheless, though plausible and intuitively appealing, additional observations of material motion within the press are needed in order to confirm this interpretation of the discrepancy in the solid flux and its resolution.

3.5.2 Clay

The details of the laboratory-scale press used by Shirato *et al.* [11] are provided in Appendix B.2. Pressure measurements are reported at six locations along the press during normal operation of dewatering of a clay slurry. These measurements, along with the fits of Shirato *et al.* [11] for $p_Y(\phi)$ and $k(\phi)$, are reproduced in figure 6. The fits are based on (uniform compaction) filtration
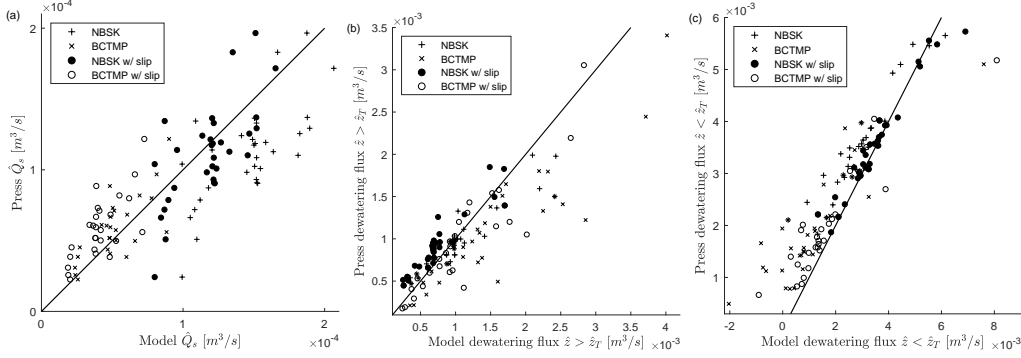
Fig. 5 Comparison between experimental press data and model results for (a): the machine solid flux, (b): dewatering flux over the shunting zone, (c): dewatering flux over the churning zone. Predictions shown for the model for NBSK ($+$) and BCTMP ($\times$) in addition to predictions accounting for slip in the shunting zone for NBSK (filled circles) and BCTMP (open circles). Solid lines show 1:1 correspondence.
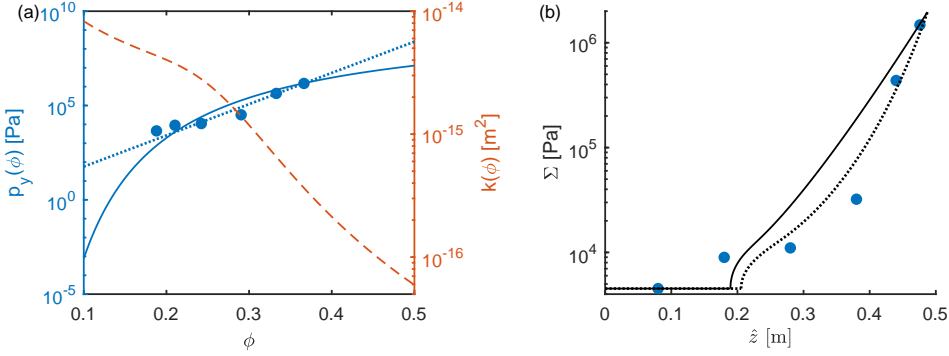
Fig. 6 (a): The fits of Shirato *et al.* [11] to $p_Y(\phi)$ (solid blue) and $k(\phi)$ (dashed red) for a clay slurry. Inferred data for $p_Y(\phi)$ from dewatering pressure profiles (blue dots); an alternative exponential fit to this data is shown as the dotted (blue) line. (b): Pressure readings at different locations along the press for dewatering of a clay slurry (blue dots) and model predictions using either the fit for $p_Y(\phi)$ of Shirato *et al.* [11] (solid) or the exponential fit (69) to the inferred $p_Y(\phi)$ points (dotted).

theory [22], and are quoted in appendix B.2. The observed pressure profile increases moderately over the first two thirds of the press before increasing rapidly over the final third, suggesting a visual identification of the transition point between churning and shunting. The rotation rate is $\Omega = 0.461 rad/s$, and the inlet is reported as being 'gravity fed' but the gravitational head is not specified. We therefore assume p_{in} to be the value of the first pressure recording in the press data of figure 6(b). The counter pressure is also not specified, but the outlet solid volume fraction $\phi_{out} = 0.379$ is, and so we set $p_{out} = p_Y(\phi_{out})$, ignoring any rate-dependent stress effect.

Model results using this calibration and no solid viscosity are included in figure 6(b). The two-part theoretical pressure profile qualitatively reproduces the data. Because there is no rate-dependent stress reported for the clay slurry, the results are sensitive to the form of $p_Y(\phi)$. For example, the alternative exponential fit

$$p_Y(\phi) = 1.272 \exp(38.13\phi) \qquad (69)$$

reproduces the pressure observations slightly better, whilst providing similar values for $p_Y(\phi)$ over the range of solid fraction encountered in the press (see figure 6(a)). This alternative fit is

suggested by estimating point values of $p_Y(\phi)$ from the pressure observations and then using the outlet solid volume fraction and the geometry change through the press to determine the solid fractions at the corresponding observation points; these estimates are included in figure 6(a).

4 Conclusions

In this paper we have proposed a model for two-phase flow in a dewatering screw press in which, following previous experimental observations [2,11,9] and modeling approaches [8,10], the press is split into two zones: a 'churning' rotational zone at the constant pressure of the inlet, followed by a 'shunting' zone of largely axial transport over which consolidation is opposed by the effective solid network stress. Unlike most previous approaches, the shunting zone is treated as a two-phase flow problem, and then simplified by exploiting the slowly varying helical geometry of the press. In the reduction, the radial pressure and solid fraction gradients dominate the consolidation dynamics, and dewatering occurs locally at each cross-section of the helical channel of the press. Variations along the helical channel become equivalent to the time evolution of a self-contained filtration process, with an explicitly prescribed axial shunting velocity through the shunting zone. In fact, the model can be simplified further to recover precisely that of a fixed-rate filtration device (*cf.* [13,14]). We perform this additional simplification in Appendix C, pointing out how the recovered filtration model has the novelty that compression occurs bi-axially and allows for a richer solid rheology than is customarily adopted.

A critical additional detail of the unsimplified screw-press model is that the transition point between churning and shunting is dictated by the force balances, with the pressure set at the inlet and the counter pressure maintained at the press exit. This further determines the solid flux through the press, and the dewatering profiles along it. In general, for a pulp suspension, the transition point is roughly set by the combination $\sqrt{p_{out}/p_{in}}$ and the solid flux is proportional to $\sqrt{\Omega p_{out}}$, where Ω is the rotation rate of the press and p_{in} and p_{out} are the inlet and oulet pressures. Such estimates for these output parameters can inform the successful operation of a screw press, and may provide indicators of when jamming or wet flushing of the press might occur.

Importantly, we compared the predictions of the model with two different screw presses operating with rather different suspensions: a pilot-scale industrial screw press dewatering cellulose fibre suspensions [12], and a laboratory-scale press used by Shirato *et al.* [11] for a clay slurry. Data collected from the pulp press, for two different suspensions and a range of operating parameters, compare well with the model predictions, especially when allowing for the possibility that a small amount of rotation may occur over the shunting zone. Although rather less data is provided by Shirato *et al.* [11], which limits the comparison, the model again appears to perform adequately.

Finally, we note that the simplified model for bi-axial compression can be taken much further in order to explore design principles as well as the generic behaviour of a screw press. In particular, for illustration in Appendix C, we investigate how the power consumption and maximum compressive load depends on the mode of compression (convergence of the flight versus expansion of the shaft) as the compaction rate is increased. The conclusion is that the expansion of the shaft usually outperforms the convergence of the flight, in that the former consumes less power and generates lower loads.

A Calculus of the coordinate transformation

A.1 Basis vectors

A general position vector written in the local helical coordinates with respect to the Cartesian basis vectors $(\hat{\mathbf{x}}, \hat{\mathbf{y}}, \hat{\mathbf{z}})$ is given by

$$\mathbf{x} = \hat{r}\cos(\varphi)\hat{\mathbf{x}} + \hat{r}\sin(\varphi)\hat{\mathbf{y}} + (\hat{\xi} + \hat{\beta}(\varphi))\hat{\mathbf{z}}. \tag{70}$$

The un-normalised basis vectors of the local helical coordinates are given by $\mathbf{e}_i = \partial\mathbf{x}/\partial x^i$, so that

$$\mathbf{e}_r = \frac{\partial\mathbf{x}}{\partial\hat{r}} = \cos(\varphi)\hat{\mathbf{x}} + \sin(\varphi)\hat{\mathbf{y}}, \tag{71}$$

$$\mathbf{e}_\varphi = \frac{\partial\mathbf{x}}{\partial\varphi} = -\hat{r}\sin(\varphi)\hat{\mathbf{x}} + \hat{r}\cos(\varphi)\hat{\mathbf{y}} + \hat{\beta}'(\varphi)\hat{\mathbf{z}}, \tag{72}$$

$$\mathbf{e}_\xi = \frac{\partial\mathbf{x}}{\partial\hat{\xi}} = \hat{\mathbf{z}}, \tag{73}$$

The normalised unit vectors $(\hat{\mathbf{e}}_r, \hat{\mathbf{e}}_\varphi, \hat{\mathbf{e}}_\xi)$ can be obtained *via* $\mathbf{e}_i = h_i\hat{\mathbf{e}}_i$ (no summation), where the scale-factors h_i are given by $(h_r, h_\varphi, h_\xi) = (1, A(\hat{r}, \varphi), 1)$, and

$$A(\hat{r}, \varphi) = \sqrt{\hat{r}^2 + \hat{\beta}'(\varphi)^2}. \tag{74}$$

The vectors $\mathbf{e}_i$ are the covariant basis vectors for this coordinate system. We will also make use of the contravariant basis vectors $\mathbf{e}^i$ defined such that $\mathbf{e}^i \cdot \mathbf{e}_j = \mathbf{e}_j \cdot \mathbf{e}^i = \delta^i_j$, where δ^i_j is the Kronecker delta symbol. It is straightforward to verify that the contravariant basis vectors are given by

$$\mathbf{e}^r = \cos(\varphi)\hat{\mathbf{x}} + \sin(\varphi)\hat{\mathbf{y}}, \tag{75}$$

$$\mathbf{e}^\varphi = -\frac{1}{\hat{r}}[\sin(\varphi)\hat{\mathbf{x}} - \cos(\varphi)\hat{\mathbf{y}}], \tag{76}$$

$$\mathbf{e}^\xi = \frac{\hat{\beta}'(\varphi)}{\hat{r}}[\sin(\varphi)\hat{\mathbf{x}} - \cos(\varphi)\hat{\mathbf{y}}] + \hat{\mathbf{z}}. \tag{77}$$

We also introduce the two metric tensors $g_{ij} = \mathbf{e}_i \cdot \mathbf{e}_j$ and $g^{ij} = \mathbf{e}^i \cdot \mathbf{e}^j$, so that

$$[g_{ij}] = \begin{pmatrix} 1 & 0 & 0 \\ 0 & A^2 & \hat{\beta}' \\ 0 & \hat{\beta}' & 1 \end{pmatrix}, \quad [g^{ij}] = \begin{pmatrix} 1 & 0 & 0 \\ 0 & \hat{r}^{-2} & -\hat{\beta}'\hat{r}^{-2} \\ 0 & -\hat{\beta}'\hat{r}^{-2} & A^2\hat{r}^{-2} \end{pmatrix}. \tag{78}$$

Finally, we must compute the Christoffel symbols Γ^k_{ij}, defined by $\partial\mathbf{e}_i/\partial x^j = \Gamma^k_{ij}\mathbf{e}_k$ (summing over k). The only non-zero symbols are

$$\Gamma^2_{12} = \Gamma^2_{21} = \frac{1}{\hat{r}}, \quad \Gamma^3_{12} = \Gamma^3_{21} = -\frac{\hat{\beta}'}{\hat{r}}, \quad \Gamma^1_{22} = -\hat{r}, \quad \Gamma^3_{22} = \hat{\beta}'', \tag{79}$$

where we associate $(1 \mapsto r, 2 \mapsto \varphi, 3 \mapsto \xi)$.

A general vector $\mathbf{v}$ can be written either as $\mathbf{v} = v^i\mathbf{e}_i$ or as $\mathbf{v} = v_i\mathbf{e}^i$. The physical components of $\mathbf{v}$ are most readily obtained via $\hat{v}^i = h_i v^i$ (no summation). Additionally, we may convert between the two components using the metric tensors, $v_i = g_{ij}v^j$ and $v^i = g^{ij}v_j$.

A.2 Calculus

To write the equations of motion (1–4) in terms of the local coordinate system, we require the gradient of a scalar ψ, the divergence of a vector $\mathbf{v}$, and the divergence of a tensor $\boldsymbol{S}$. First, we have that

$$\hat{\boldsymbol{\nabla}}\psi = \frac{\partial\psi}{\partial x_i}\mathbf{e}^i, \tag{80}$$

so that $(\hat{\boldsymbol{\nabla}}\psi)_i = \partial\psi/\partial x_i$. To find the physical components of $\hat{\boldsymbol{\nabla}}\psi$ we first identify $(\hat{\boldsymbol{\nabla}}\psi)^i$ and use the scale factors h_i to find

$$\hat{\boldsymbol{\nabla}}\psi = \frac{\partial\psi}{\partial\hat{r}}\hat{\mathbf{e}}_r + \left[\frac{A}{\hat{r}^2}\frac{\partial\psi}{\partial\varphi} - \frac{A\hat{\beta}'}{\hat{r}^2}\frac{\partial\psi}{\partial\hat{\xi}}\right]\hat{\mathbf{e}}_\varphi + \left[\frac{A^2}{\hat{r}^2}\frac{\partial\psi}{\partial\hat{\xi}} - \frac{\hat{\beta}'}{\hat{r}^2}\frac{\partial\psi}{\partial\varphi}\right]\hat{\mathbf{e}}_\xi \tag{81}$$

Next, we have that

$$\hat{\boldsymbol{\nabla}} \cdot \mathbf{v} = \frac{\partial v^i}{\partial x_i} + v^k \Gamma^i_{ki} = \frac{\partial v^r}{\partial \hat{r}} + \frac{v^r}{\hat{r}} + \frac{\partial v^\varphi}{\partial \hat{\varphi}} + \frac{\partial v^\xi}{\partial \hat{\xi}}, \tag{82}$$

or in terms of physical components,

$$\hat{\boldsymbol{\nabla}} \cdot \mathbf{v} = \frac{1}{\hat{r}} \frac{\partial}{\partial \hat{r}} (\hat{r} \hat{v}^r) + \frac{\partial}{\partial \varphi} \left(\frac{\hat{v}^\varphi}{A} \right) + \frac{\partial \hat{v}^\xi}{\partial \hat{\xi}}. \tag{83}$$

Finally, we consider tensors written in the form $\boldsymbol{S} = S^{ij} \mathbf{e}_i \mathbf{e}_j$, so that the physical components are given by $\hat{S}^{ij} = h_i h_j S^{ij}$ (no summation). We have that

$$\hat{\boldsymbol{\nabla}} \cdot \boldsymbol{S} = \left[\frac{\partial S^{ij}}{\partial x^j} + S^{mj} \Gamma^i_{mj} + S^{im} \Gamma^j_{mj} \right] \mathbf{e}_i. \tag{84}$$

In physical components, this becomes

$$\begin{aligned}
\hat{\boldsymbol{\nabla}} \cdot \boldsymbol{S} = {}& \left[\frac{\partial \hat{S}^{rr}}{\partial \hat{r}} + \frac{\partial}{\partial \varphi} \left(\frac{\hat{S}^{r\varphi}}{A} \right) + \frac{\partial \hat{S}^{r\xi}}{\partial \hat{\xi}} + \frac{\hat{S}^{rr}}{\hat{r}} - \frac{\hat{r} \hat{S}^{\varphi\varphi}}{A^2} \right] \hat{\mathbf{e}}_r \\
& + \left[A \frac{\partial}{\partial \hat{r}} \left(\frac{\hat{S}^{\varphi r}}{A} \right) + A \frac{\partial}{\partial \varphi} \left(\frac{\hat{S}^{\varphi\varphi}}{A^2} \right) + \frac{\partial \hat{S}^{\varphi\xi}}{\partial \hat{\xi}} + \frac{\hat{S}^{r\varphi}}{\hat{r}} + 2 \frac{\hat{S}^{\varphi r}}{\hat{r}} \right] \hat{\mathbf{e}}_\varphi \\
& + \left[\frac{\partial \hat{S}^{\xi r}}{\partial \hat{r}} + \frac{\partial}{\partial \varphi} \left(\frac{\hat{S}^{\xi\varphi}}{A} \right) + \frac{\partial \hat{S}^{\xi\xi}}{\partial \hat{\xi}} - \frac{\hat{\beta}' \left(\hat{S}^{r\varphi} + \hat{S}^{\varphi r} \right)}{A\hat{r}} + \frac{\hat{\beta}'' \hat{S}^{\varphi\varphi}}{A^2} + \frac{\hat{S}^{\xi r}}{\hat{r}} \right] \hat{\mathbf{e}}_\xi.
\end{aligned} \tag{85}$$

It is straightforward to demonstrate that this reduces to the formula for cylindrical polar coordinates for which $\hat{\beta} = 0$ and $A = \hat{r}$. For the case of an isotropic tensor $\boldsymbol{S} = \hat{S}\boldsymbol{I}$, this formula reduces to

$$\hat{\boldsymbol{\nabla}} \cdot (\hat{S}\boldsymbol{I}) = \left(\frac{\partial \hat{S}}{\partial \hat{r}} + \frac{(\hat{\beta}')^2 \hat{S}}{\hat{r} A^2} \right) \hat{\mathbf{e}}_r + A \frac{\partial}{\partial \varphi} \left(\frac{\hat{S}}{A^2} \right) \hat{\mathbf{e}}_\varphi + \left(\frac{\partial \hat{S}}{\partial \hat{\xi}} + \frac{\hat{\beta}'' \hat{S}}{A^2} \right) \hat{\mathbf{e}}_\xi. \tag{86}$$

An important limiting case for the above calculations is that of a constant pitch helix, so that $\hat{\beta}(\varphi) = \hat{l}\varphi/2\pi$ and $\hat{\beta}'' = 0$. We may then introduce the pitch angle $\alpha(\hat{r})$ given by $\tan(\alpha) = \hat{l}/2\pi\hat{r}$, so that $\hat{\beta}' = \hat{r}\tan(\alpha)$ and $A = \hat{r}\sec(\alpha)$. This allows the above formulae to be written in terms of $\hat{r}$ and α only, extending previous work with constant pitch helices [16] by adding the tensor divergence.

B Details of press geometries and experiments

B.1 UQTR's pulp pressing

Pilot-plant trials of a screw press were performed at the University of Quebec Three Rivers (UQTR) and reported in [12] for two different pulp suspensions. The trials systematically varied the inlet pressure p_{in}, counter pressure p_{out}, and shaft rotation rate Ω, and measured as output variables the solid flux through the press, the solid volume fraction of material leaving the press, four pressure measurements at fixed locations along the press, and dewatering flow rates collected over fourteen intervals along the press. The two pulp suspensions we compare to are Northern Bleached Softwood Kraft (NBSK) and Bleached Chemi-Thermo-Mechanical Pulp (BCTMP). The compressive yield stress $p_Y(\phi)$ and permeability $k(\phi)$ for each pulp, calibrated following the procedure outlined in [14], are shown in figure 7. For each material we take the bulk viscosity to be $\hat{\Lambda}(\phi) = \eta\phi^2$ as in [14] where $\eta = 10^7$ Pa sec for NBSK and 3.2×10^8 Pa sec for BCTMP.

The geometry of the press itself is shown in figure 1 and consists of a $1.45m$ long shaft which expands over an intermediate region of its full extent. The pitch of the flight also slowly decreases along the length of the press. The geometrical parameters used in our model comparison are

$$\hat{r}_w(\hat{z}) = \begin{cases} 0.039 & \text{for } 0 \le \hat{z} < 0.45 \\ 0.038(\hat{z} - 0.45) + 0.039 & \text{for } 0.45 \le \hat{z} < 1.39 \,, \\ 0.075 & \text{for } 1.39 \le \hat{z} < 1.45 \end{cases} \tag{87}$$

$$\hat{\beta}(\varphi) = 0.015 + 0.042\varphi - 0.000275\varphi^2. \tag{88}$$
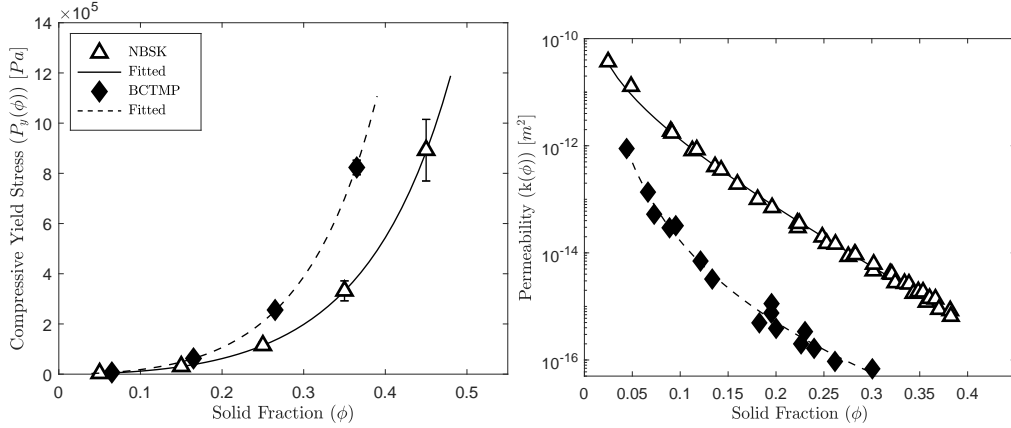
Fig. 7 Measurements and fits to compressive yield stress $p_Y(\phi)$ (left) and permeability $k(\phi)$ (right) for NBSK and BCTMP pulps. The fit uses $p_Y(\phi) = a\phi^b/(1-\phi)^c$ with $(a, b, c) = (0.6\text{MPa}, 1.84, 3.12)$ for NBSK and $(1.09\text{MPa}, 1.96, 3.39)$ for BCTMP. For $k(\phi)$ the fits are $k(\phi) = A\log(1/\phi)\exp(-B\phi)/\phi$ with $(A, B) = (3.6 \times 10^{-13}\text{m}^2, 18.52)$ for NBSK and $(1.62 \times 10^{-14}\text{m}^2, 22.91)$ for BCTMP.

The basic pitch is therefore $\hat{l} \approx 0.27m$, and the presence of φ^2 in $\hat{\beta}(\varphi)$ (with a negative coefficient) represents the gradual reduction of the pitch over the eight turns of the flight. The basket radius is $r_b = 0.115m$ and the small geometrical parameter is $\delta \approx 0.014$.

The trials varied the rotation rates in the range $\Omega \in [2.23, 4.63]rad/s$, inlet pressures $p_{in} \in [9.2, 30.2]kPa$, and counter pressures $p_{out} \in [200, 400]kPa$.

B.2 Clay pressing of Shirato *et al.* [11]

Shirato *et al.* [11] consider screw press dewatering of a clay slurry. The dewatering length of their press is $0.499m$ and is represented by the geometrical functions

$$\hat{r}_w(\hat{z}) = 7.48 \times 10^{-3}\hat{z} + 6 \times 10^{-3}, \tag{89}$$

$$\hat{\beta}(\varphi) = 3.72 \times 10^{-3}\varphi. \tag{90}$$

The flights do not converge along the 22 turns of the flight; the constant pitch is $\hat{l} = 0.0234m$. The basket radius is $r_b = 12mm$ and the shaft slowly expands from $\hat{r}_w = 6mm$ to $10mm$. The small parameter is $\delta \approx 2.3 \times 10^{-4}$.

The calibration according to the methodology of Ruth [22] of $p_Y(\phi)$ and $k(\phi)$ for their Clay slurry is quoted as

$$p_Y(\phi) = 98.0665 \exp\left(\frac{6.01 - 1/\phi}{0.34}\right), \tag{91}$$

$$k(\phi) = \frac{1}{23450\phi\{1.65 \times 10^8 \exp[0.776(6.01 - 1/\phi)/0.34] + 5.14 \times 10^{10}\}}. \tag{92}$$

C A model for bi-axial compression

In this appendix we consider a further simplification of the screw-press model in which the gap of the helical channel becomes sufficiently small that all curvature effects become negligible. We also ignore the churning section and consider only the dynamics of the shunting zone. In this circumstance, the model collapses to that for a fixed-rate filtration problem in a rectangular box, with the along-press coordiante q playing the role of time. The box may compress bi-axially, however, either by a reduction of its height or width, which divorces the problem from previous models of filtration [13, 14]. With the current model we investigate the effects of the ratio of width-reduction and height-reduction rates on the dewatering dynamics in order to draw general conclusions about optimal press design. However, as a novel model for bi-axial filtration, the analysis is self contained and not only applicable to a screw press, leading us to present a somewhat general discussion.
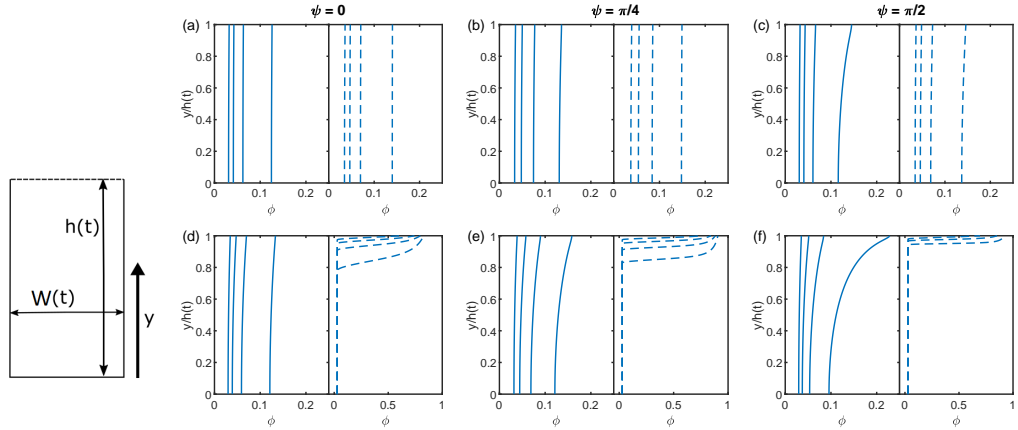
Fig. 8 A schematic of the simplified bi-axial compression model. Solid fraction profiles ϕ against $y/h(t)$ for bi-axial compression with $\psi = 0$ (a,d), $\psi = \pi/4$ (b,e) and $\psi = \pi/2$ (c,f) for each of $\gamma = 100$ (a-c) and $\gamma = 0.01$ (d-f). Results shown for pulp (solid) with $\phi_0 = 0.025$ and nylon (dashed) with $\phi_0 = 0.028$ at times $t = 0.2, 0.4, 0.6$ and 0.8.

C.1 Further simplification of the screw-press model

When the gap between the shaft and the basket is relatively narrow, the helical coordinates reduce (locally) to Cartesian coordinates describing each cross-section. If we further replace q explicitly by a time-like coordinate t, then the model for the shunting zone simplifies to

$$\frac{\partial \phi}{\partial t} + \frac{\partial(\phi u)}{\partial y} + \frac{\dot{W}}{W}\phi = 0, \tag{93}$$

$$u = -\frac{\dot{W}}{W}y - \gamma K(\phi)\frac{\partial P}{\partial y}, \tag{94}$$

for a two-dimensional box of width $W(t)$, in which the vertical coordinate is $0 < y < h(t)$, and the upper surface $y = h(t)$ is permeable (*i.e.* W and h are equivalent to $l(1-b)$ and $1-r_w$, respectively, and $r = r_w + y$). The boundary conditions are therefore

$$u = 0 \text{ at } y = 0, \quad u = \dot{h} \text{ at } y = h(t), \quad p = 0 \text{ at } y = h(t), \tag{95}$$

where $p(y,t)$ is the pore pressure. The total compressive load is

$$\Sigma(t) = p(y,t) - P(y,t),$$

given that $\partial(P - p)/\partial y = 0$. The factor $\dot{W}/W$ represents the effect of the closing impermeable side-walls of the box (assuming once more that the material remains uniform across the width of the box).

For constant velocity bi-axial compression, we set (dimensionally) $\hat{h}(t) = -V\cos(\psi)$ and $\hat{W} = -V\sin(\psi)$, where ψ is a parameter which measures the relative motion of the side-walls to the lid. The velocity scale $V > 0$ is used to nondimensionalise the velocity fields so that the dimensionless compression time is

$$\gamma = \frac{p_* k_*}{V\mu h_0}, \tag{96}$$

where h_0 is the (dimensional) initial height of the box. We consider initially square boxes so that the dimensionless height and width of the box are $h(t) = 1 - \cos(\psi)t$ and $W(t) = 1 - \sin(\psi)t$ respectively. Note that when $\psi = 0$, only the height decreases and the model reduces to that of Hewitt *et al.* [14]. If $\psi = \pi/2$, only the side-walls compress the material and the box remains of constant height.

The effective solid network stress is given by

$$P = \Pi_Y(\phi) - \frac{\epsilon}{\gamma}\Lambda(\phi)\left(\frac{\partial u}{\partial y} + \frac{\dot{W}}{W}\right), \tag{97}$$

where the dimensionless parameter measuring the relative strength of the rate-dependent stress is given by

$$\epsilon = \frac{\eta k_*}{\mu h_0^2}, \tag{98}$$

and η is the dimensional scale of the bulk viscosity function $\hat{\Lambda}(\phi)$.

Figure 8 shows example solutions to the bi-axial compression model for suspensions compressed using $\psi = 0$, $\pi/4$, and $\pi/2$. The figure shows the behaviour of relatively slow compaction with $\gamma = 100$ and relatively fast compaction with $\gamma = 0.01$. For each case, examples are given for a material with a rate-dependent stress given by $\Lambda(\phi) = \phi^2$, or a material without solid bulk viscosity, $\epsilon = \Lambda(\phi) = 0$. The rate-dependent material corresponds to the pulp suspensions used in considering the full screw-press model, with the functional forms of $\Pi_Y(\phi)$ and $K(\phi)$ given by the empirical fits found by [14], and an initial solid fraction of $\phi_0 = 0.025$; we take $\epsilon = 7$ (which roughly corresponds to NBSK pulp compacted from an initial height $h_0 = 5.5$cm). For the rate-indendent material we use the fits for $\Pi_Y(\phi)$ and $K(\phi)$ found for a suspension of nylon fibres [14], and we set $\phi_0 = 0.028$.

The figure shows profiles of solid volume fraction at times $t = 0.2$, 0.4, 0.6 and 0.8 during the compression. We see that for slow compaction at $\gamma = 100$, the profiles of solid volume fraction remain relatively uniform, with a slight deviation at later times which is particularly clear for width-only compaction, $\psi = \pi/2$. For rapid compression, although the bulk viscosity $\Lambda(\phi)$ aids in maintaining the uniformity of the pulp suspension, the lack of a bulk viscosity for nylon fibres results in a boundary layer developing against the permeable surface at $y = h(t)$. Notably, this boundary layer is thinner and attains higher values of ϕ for width-only compaction, $\psi = \pi/2$. Evidently, over a wide range of values of γ, compression via the side walls alone, $\psi = \pi/2$, results in 'worse' dewatering behaviour in the sense that higher solid volume fractions, and therefore larger compressive loads, develop against the permeable screen.

C.2 Optimal bi-axial compression

To quantify further the effect of the mode of compression, in figure 9 we plot the (dimensionless) power $\mathcal{W}(\psi)$ required to compact from an initial solid volume fraction of $\phi_0 = 0.025$ to an average final solid volume fraction of $\overline{\phi} = 0.12$ as a function of ψ for an NBSK pulp suspension for various values of γ. The power is given by

$$\mathcal{W}(\psi) = \int_{0.025}^{0.12} 2P(h, t)|\dot{h}w + \dot{w}h|\, \mathrm{d}\overline{\phi}, \tag{99}$$

and the figure shows the power normalised by that used when $\psi = 0$, i.e. by $\mathcal{W}(0)$. The power increases with ψ, with compression via the side walls using the most power. Additionally, this dependence on ψ is exaggerated as γ is reduced; when $\gamma = 0.001$, width-only compaction consumes around three times as much power as height-only compaction.

In terms of press design, the value $\psi = \pi/4$ represents the shortest length of press for a given area contraction. Figure 9 shows that this choice of ψ consumes approximately the same amount of power as any $\psi < \pi/4$, which all represent longer press lengths. This points towards an optimal design of equal rates of geometry reduction due to shaft expansion and the convergence of the helical flight. Additionally, we note that a flight which induces geometry reductions more rapidly than the expanding shaft not only requires a longer press but also consumes more power and reaches higher peak loads. The inset demonstrates that the power usage increases rapidly as γ is decreased, with the scaling $\mathcal{W}(0) \propto \gamma^{-1}$ emerging as $\gamma \to 0$. Notably, for each value of γ, the power consumption remains roughly constant for $0 \le \psi \le \pi/4$, with the dependence on the mode of compression emerging for $\psi > \pi/4$. Most strikingly, as $\gamma \to 0$, the curves $\mathcal{W}(\psi)/\mathcal{W}(0)$ collapse onto a single line independently of γ.

C.3 Nearly uniform compression

For slow compaction ($\gamma \gg 1$), the material remains nearly uniform during consolidation, suggesting that there should be no distinction between the different modes of compression. However, even for $\gamma = 100$, we observe a slight difference between height-only ($\psi = 0$) and width-only ($\psi = \pi/2$) compaction. To further investigate this limit, we repeat the analysis of §3.2, which leads to

$$\left(\frac{\dot{h}}{h} + \frac{\dot{W}}{W}\right) y = -\gamma B'(\phi)\frac{\partial \phi}{\partial y}, \tag{100}$$
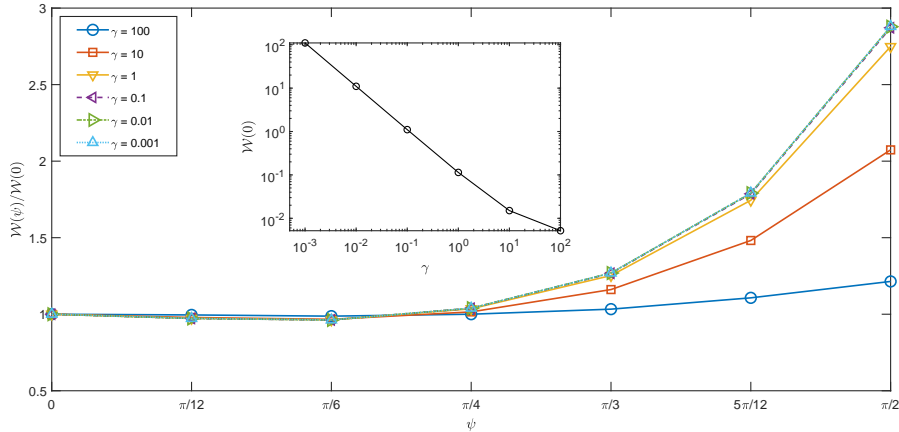
Fig. 9 Power consumption $\mathcal{W}(\psi)$ normalised by $\mathcal{W}(0)$ during consolidation from $\phi_0 = 0.025$ to average solid volume fraction $\overline{\phi} = 0.12$ as a function of ψ. Plots for an NBSK pulp suspension with $\epsilon = 7$ for $\gamma = 100$ (dark blue circles), 10 (red squares), 1 (yellow downward triangles), 0.1 (purple leftward triangles), 0.01 (green rightward triangles) and 0.001 (light blue upward triangles). Inset shows power consumption when $\psi = 0$, $W(0)$, against γ.

in place of (52), and we have assumed $\epsilon \ll \gamma$ to simplify the constitutive law. Thence, expanding around the uniform solution $\overline{\phi}$ and applying the total mass constraint, we integrate to find

$$\phi \approx \overline{\phi} + \left| \frac{\dot{h}}{h} + \frac{\dot{W}}{W} \right| \frac{y^2 - h^2/3}{2\gamma B'(\overline{\phi})}, \tag{101}$$

implying that the solid fraction at the permeable screen is given by

$$\phi(h(t), t) = \frac{\phi_0}{wh} + \left(\frac{\cos(\psi)}{1 - \cos(\psi)t} + \frac{\sin(\psi)}{1 - \sin(\psi)t} \right) \frac{[1 - \cos(\psi)t]^2}{3\gamma B'(\overline{\phi})}, \tag{102}$$

which increases with ψ and sets the total load, since $|\Sigma| \sim \Pi_Y(\phi(h, t))$ in this limit.

For compaction purely through changes in h ($\psi = 0$), the departure of $\phi(h, t)$ from $\overline{\phi} = \phi_0/wh$ is a factor of $(1 - t)^2$ smaller than that for compaction purely through changes in w ($\psi = \pi/2$). Intuitively, as ψ increases, the height of the domain remains larger for longer, and so gradients in ϕ are able to more easily develop over time, thus leading to increased loads and power consumption.

The improved prediction for the solid fraction in (54) is now replaced by

$$B(\phi) = B(\phi_{y=0}) + \gamma^{-1} \left| \frac{\dot{h}}{h} + \frac{\dot{W}}{W} \right| \frac{y^2}{2}. \tag{103}$$

Examples of dynamics for width-only compaction, $\psi = \pi/2$, and with $\gamma = 100$ following the solution (103) and departures from it, are shown in figure 10. The full solution for nylon is always well-represented by (103). For pulp, there is no solution to (103) which accommodates the total mass constraint at $t = 0.85$.

C.4 Rapid compaction

For rapid compaction, $\gamma \ll 1$, the effective solid network stress is dominated by the rate-dependent term, that is

$$P \sim -\frac{\epsilon}{\gamma} \Lambda(\phi) \left(\frac{\partial u}{\partial y} + \frac{\dot{W}}{W} \right). \tag{104}$$

Upon substituting this limiting form into Darcy's law (94) we see that γ drops out of the dynamics in the small γ limit. Additionally, the power reduces to $\mathcal{W}(\psi) \propto \epsilon/\gamma$, which rationalises the scaling $\mathcal{W}(0) \propto \gamma^{-1}$ evident in the inset in figure 9. Given that the detailed dynamics also become independent of γ (since it also drops out of Darcy's law), it is clear that γ drops out of $\mathcal{W}(\psi)/\mathcal{W}(0)$ when $\gamma \ll 1$. Dimensionally, the effective solid network stress is $\hat{S} = -p_* P \propto V\eta/h_0$ for rapid compaction, and so the power consumption becomes proportional to the compaction rate V.
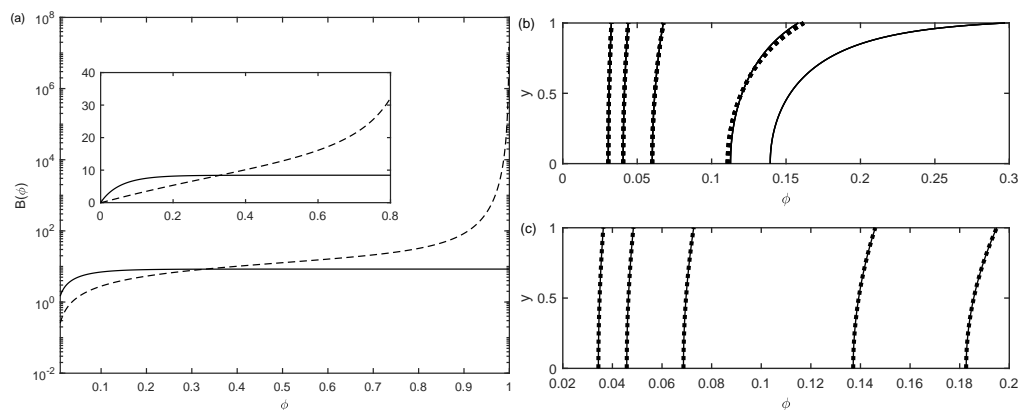
Fig. 10 (a): The function $B(\phi) = \int K(\Phi)\Pi'_Y(\Phi)\,d\Phi$ for pulp (solid) and nylon (dashed). (b,c): Solidity profiles for width-only compaction ($\psi = \pi/2$) with $\gamma = 100$ for (b) pulp and (c) nylon. Solutions to the full problem (solid) initialised from a solution to (103) with $\bar{\phi} = 0.025$ (pulp) and 0.028 (nylon) and solutions to (103) (dots) at times $t = 0.2, 0.4, 0.6, 0.7, 0.8$ and 0.85. For pulp, there is no solution to (103) at $t = 0.85$.

References

1. H. G. Schwartzberg. Expression of fluid from biological solids. *Sep. Purif. Rev.*, 26:1–213, 1997.
2. J. A. Ward. Processing high oil content seeds in continuous screw presses. *J. Am. Oil Chem. Soc.*, 53:261–264, 1976.
3. J. Singh and P. C. Bargale. Development of a small capacity double stage compression screw press for oil expression. *J. Food Eng.*, 43:75–82, 2000.
4. M. Shirato, T. Murase, and M. Iwate. Pressure profile in a power-law fluid in constant-pitch, straight-taper and decreasing pitch screw extruders. *Int. Chem. Eng.*, 23:323–332, 1983.
5. F. Wang and A. Melson. Canola paste extrusion for feeding supercritical extractors. *Can. J. Phys.*, 73:304–309, 1995.
6. Q. Yu and G.-H. Hu. Development of a helical coordinate system and its application to analysis of polymer flow in screw extruders. Part I. The balance equations in a helical coordinate system. *J. Non-Newtonian Fluid Mech.*, 69:155–167, 1997.
7. Y. Béreaux, M. Moguedet, X. Raoul, J. Y. Charmeau, J. Balcaen, and D. Graebling. Series solutions for viscous and viscoelastic fluids flow in the helical rectangular channel of an extruder screw. *J. Non-Newtonian Fluid Mech.*, 123:237–257, 2004.
8. V. S. Vadke, F. W. Sosulski, and C. A. Shook. Mathematical simulation of an oilseed press. *J. Am. Oil Chem. Soc.*, 65:1610–1616, 1988.
9. T. O. Omobuwajo, M. T. Ige, and A. O. Ajayi. Theoretical prediction of extrusion pressure and oil flow rate during screw expeller processing of palm kernel seeds. *J. Food Eng.*, 38:469–485, 1999.
10. P. Willems, N. J. M. Kuipers, and A. B. de Haan. A consolidation based extruder model to explore GAME process configurations. *J. Food Eng.*, 90:238–245, 2009.
11. M. Shirato, T. Murase, N. Hayashi, K. Miki, T. Fukushima, T. Suzuki, N. Sakakibara, and T. Tazima. Fundamental studies on continuous extrusion using a screw press. *Int. Chem. Eng.*, 18:680–688, 1978.
12. B. El Idrissi, E. Loranger, R. Lanouette, J.-P. Bousquet, and D. M. Martinez. Dewatering parameters in a screw press and their influence on the screw press outputs. *Chem. Eng. Res. Des.*, 152:300–308, 2019.
13. K. A. Landman, C. Sirakoff, and L. R. White. Dewatering of flocculated suspensions by pressure filtration. *Phys. Fluids A*, 3:1495–1509, 1991.
14. D. R. Hewitt, D. T. Paterson, N. J. Balmforth, and D. M. Martinez. Dewatering of fibre suspensions by pressure filtration. *Phys. Fluids*, 28:063304, 2016.
15. D. Paterson, T. S. Eaves, D. R. Hewitt, N. J. Balmforth, and D. M. Martinez. Flow-driven compaction of a fibrous porous medium. *Phys. Rev. Fluids*, 4:074306, 2019.
16. R. A. Waldron. A helical coordinate system and its applications in electromagnetic theory. *Quart. J. Mech. Appl. Math.*, 11:438–461, 1958.
17. G. K. Batchelor. *An Introduction to Fluid Dynamics*. Cam. Univ. Press, 1967.
18. K. Terzaghi. *Theoretical soil mechanics*. Wiley, 1943.
19. D. A. Drew. Mathematical modeling of two-phase flow. *Ann. Rev. Fluid Mech.*, 15:261–291, 1983.

20. R. Buscall and L. R. White. The consolidation of concentrated suspensions. Part I. The theory of sedimentation. *Phys. Chem. Cond. Phas.*, 83:873–891, 1987.
21. V. Lobosco and V. Kaul. An elastic/viscoplastic model of the fibre network stress in wet pressing: Part 1. *Nord. Pulp Pap. Res. J.*, 16:12–17, 2001.
22. B. F. Ruth. Studies in filtration III. Derivation of general filtration equations. *Ind. Eng. Chem.*, 27:708–723, 1935.